Viscous control of cellular respiration by membrane lipid composition

Authors: Itay Budin[1,2*], Tristan de Rond[1,3†], Yan Chen[1,6], Leanne Jade G. Chan[1‡], Christopher J. Petzold[1,6], and Jay D. Keasling[1,2,4-8*]

Affiliations:

[1.] Joint BioEnergy Institute, 5885 Hollis Street, Emeryville, CA 94608

[2.] Department of Chemical & Biomolecular Engineering, University of California, Berkeley, Berkeley CA 94720

[3.] Department of Chemistry, University of California, Berkeley, Berkeley, CA 94720

[4.] Department of Bioengineering, University of California, Berkeley, Berkeley CA 94720

[5.] QB3 Institute, University of California, Berkeley, Berkeley, CA 94270

[6.] Biological Systems & Engineering, Lawrence Berkeley National Laboratory, Berkeley, CA 94720

[7.] The Novo Nordisk Foundation Center for Sustainability, Technical University of Denmark, Denmark

[8.] Center for Synthetic Biochemistry, Institute for Synthetic Biology, Shenzhen Institutes for Advanced Technologies, Shenzhen, CN

* Correspondence to: keasling@berkeley.edu, budin@berkeley.edu

† Current address: Scripps Institution of Oceanography, University of California, San Diego

‡ Current address: Calico Life Sciences

Abstract: Lipid composition determines the physical properties of biological membranes and can vary substantially between and within organisms. We describe a specific role for the viscosity of energy-transducing membranes in cellular respiration. Engineering of fatty acid biosynthesis in *Escherichia coli* allowed us to titrate inner membrane viscosity across a 10-fold range by controlling the abundance of unsaturated or branched lipids. These fluidizing lipids tightly controlled respiratory metabolism, an effect that can be explained with a quantitative model of the Electron Transport Chain (ETC) that features diffusion-coupled reactions between enzymes and electron carriers (quinones). Lipid unsaturation also modulated mitochondrial respiration in engineered budding yeast strains. Thus, ETC mobility may serve as an evolutionary constraint for lipid composition in respiratory membranes.

One Sentence Summary: The viscosity of the bacterial inner membrane regulates cellular respiration, leading to a diffusion-coupled reaction model for the Electron Transport Chain.

Main Text: Cell membranes contain a multitude of distinct lipid components, but understanding how specific lipids influence biological function is challenged by limited tools for their manipulation *in vivo* (*1*). Lipids can determine the physical characteristics of membranes (*2*), such as their viscosity, and these properties are homeostatically maintained by cells (*3*). In a classic example (Fig. S1), the bacterium *E. coli* increases the proportion of phospholipid acyl chains with double bonds (unsaturation) with decreasing growth temperatures, thereby maintaining a constant membrane viscosity (*4*). Similar lipid adaptations have been widely observed across organisms (*5*), suggesting that universal processes are mediated by membrane viscosity.

To investigate functions for membrane viscosity *in vivo*, we used metabolic engineering strategies to genetically modulate lipid composition in *E. coli* (Fig. S2). FabB (β-ketoacyl-[acyl carrier protein] synthase I) carries out the rate-limiting step (*6*) for production of unsaturated fatty acids (UFAs) during fatty acid (FA) biosynthesis (Fig. 1A). We replaced the chromosomal copy of *fabB* with one under control of an *L*-arabinose-induced promoter (P_{BAD}) in a strain background that allows for titratable and homogenous expression (*7*, *8*). After further tuning FabB levels with Shine-Dalgarno Sequence variants (Fig. S2C), we generated strains with controllable UFA amounts ranging from ~15% [the minimum amount for survival (*9*)] to ~ 80% of all FAs at 37 ºC (Fig. 1B). This modulation resulted primarily from the substitution of palmitate (C16:0) with vaccinate (C18:1) acyl chains (Fig. S3A), which was observed in all phospholipid species (Fig. S3B) and maintained throughout exponential growth (Fig. S3D). Membrane ordering, as measured by steady-state anisotropy of di-phenyl-hexatriene (DPH), steadily decreased with increasing lipid unsaturation in both inner membrane vesicles and protein-free liposomes (Fig. 1C). To estimate the effect of lipid unsaturation on membrane microviscosity, we measured diffusion coefficients of a nitrobenzoxadiazole (NBD) conjugated phosphoethanolamine (PE) in giant *E. coli* inner membrane vesicles (GEVs) using Fluorescence Recovery After Photobleaching (FRAP) (Fig. 1D). From these data, viscosities were derived using the Saffman-Delbrück approximation (*10*) and showed a ten-fold range (~2 to 20 Poise) as UFA content was modulated.

To identify physiological functions for UFAs, we correlated exponential growth rates with sampled lipid compositions in cells producing various amounts of FabB (Fig. 2A). Growth rates generally featured a biphasic dependence on lipid unsaturation: A sharp fitness cliff leading to a cessation of cell growth at low UFA levels [15-20% at 37 ºC, regime I], followed by increasing growth rates with higher UFA content (regime II). Regime I corresponded to the minimum amount of UFAs required (e.g., in Fig S1) and was observed under all conditions. In contrast, regime II was dependent on media with non-fermentable carbon sources, where growth is tightly coupled to ATP production through the Electron Transport Chain (ETC) (*11*). Under fermentation conditions, when cells depend on glycolysis and are resistant to respiratory uncouplers (Fig. S4D), growth rates were unaffected by UFAs in regime II (Fig. 2A). An analysis of stress response factors (Fig. 2B) showed that that low UFA levels caused both an Oxidative Stress Response (OSR), which can result from ETC inhibition (*12*), and a Heat Shock Response (HSR), which is activated by misfolded proteins (*13*). However, HSR activation occurred only as membranes approached a gel phase transition at the growth temperature (Fig. S5B), and coincided with the mislocalization of membrane proteins (Fig. S5C) and defects in cell division (Fig. S5D). We therefore concluded that increasing proportions of saturated lipids trigger envelope stress as membranes become highly ordered (regime I), but also have a second, respiratory role over a broader range of stoichiometry (regime II).

When titrating FA synthesis, cellular respiration rates were tightly coupled to changes in unsaturated lipid content (Fig. 2C). This effect was independent of electron donor (for example, succinate or glycerol), electron acceptor (oxygen or nitrate), proton motive force (PMF) uncoupling, oxygen concentration (Fig. S6A), and growth stage (Fig. S6B). Wild-type cells overproducing UFAs through *fabB* overexpression or deletion of the regulator *fabR* similarly showed increased respiratory rates (Fig. S6C). Under glucose fermentation, low lipid unsaturation led to the accumulation of pyruvate and lactate as secreted organic acids and a depletion of succinate. Such a mixed acid fermentation profile is consistent with ETC inhibition (Fig. S6D).

To test if respiratory regulation occurs through a physical effect, we engineered a heterologous system for controlling membrane viscosity based on branched-chain fatty acid (BCFA) synthesis (Fig. 2D). Introduction of the *bkd* operon (for biosynthesis of *β*-ketoacids) and *fabH* (for initiation of BCFA synthesis) from *B. subtilis* led to the accumulation of BCFAs in membrane lipids (Fig. S7A), especially when amounts of UFA were low (Fig. S7B). BCFA biosynthesis fluidized membranes (Fig. S7C) and rescued growth defects from low lipid unsaturation (Fig. S7D), even at amounts of UFAs that were otherwise lethal (Fig. S7E). Uncoupled respiration rates were increased by BCFAs in addition to UFAs, and the effects of both fatty acid species were preserved in isolated membrane vesicles (Fig. 2E).

We considered three mechanisms by which membrane viscosity could control ETC function. First, substrate uptake could be dependent on membrane properties, especially the passive permeation of oxygen. However, lipids act on respiration independently of substrate and oxygen concentrations (Fig. S6A). Alternatively, viscosity could affect the enzymatic activity of individual ETC enzymes. However, their partial activities with soluble substrates were not inhibited by saturated lipids (Fig. S6E). Lastly, we considered whether viscosity mediates collisions between electron carriers (ubiquinone) and enzyme complexes in the ETC, since a rate dependence on solvent viscosity is a hallmark of diffusion-limited reactions (*14*). Based on the pool behavior of quinones (*15*, *16*), their diffusion between complexes has been proposed to be rate-limiting in mitochondrial respiration (*17*, *18*), but this concept was disputed (*19*, *20*).

To investigate the role of diffusion in cellular respiration, we developed a model of the *E. coli* ETC based on the Brownian motion of membrane components and their collision-mediated reactions (Fig. 3A, Fig. S8). As inputs, we combined activities of purified ETC enzymes - dehydrogenases (DHs) and terminal oxidases (TOs) - with measurements of their absolute abundances using quantitative mass spectrometry (Supplementary Information) and their organization into homotypic domains as previously described (*21*, *22*). Whole cell simulations were then carried out to quantify the rate of electron transfer as a function of ubiquinone diffusivity. To measure this parameter, we used FRAP experiments with an NBD-conjugated ubiquinone (NBD-UQ, Fig. S9) to define lipid-dependent diffusion coefficients (Fig. 3B).

Our model predicted that ubiquinone diffusivity controls respiratory flux in membranes spanning the tested range of lipid compositions. Diffusion control was measured by quinone anisotropy, with reduced electron carriers becoming depleted in the vicinity of TOs (Fig. 3C, Mov. S1). As diffusion increased, the quinone pool became well-mixed and rates were increasingly determined by enzyme activities (Fig. S8B). Simulations matched measured respiratory rates when enzymes were modeled as domains of 10 to 30 proteins (Fig. 3D), consistent with their reported organization (*21*). Simulations also predicted changes to respiratory rates upon inhibition of ETC enzymes (Fig. 3E), which reduces the rate dependence

on diffusion, and during genetic titration of TO abundance (Fig. 3F), which modulates the average diffusion distance for a reactive collision.

As in bacteria, respiration in eukaryotic mitochondria is also dependent on quinone-mediated electron transfer. In animal models, correlations between mitochondrial FA composition and metabolic rate have been observed between species (*23*), and membrane-fluidizing steroids have been shown to promote respiration (*24*). To test whether lipid composition controls mitochondrial respiration, we used a set of constitutive promoters to manipulate Ole1 (stearoyl-CoA-9-desaturase) levels in *Saccharomyces cerevisiae* (Fig. 4A). In strains that showed regular mitochondrial morphology (Fig. S10A), greater lipid unsaturation led to increased respiratory activity but, as in *E. coli*, did not inhibit fermentative metabolism or growth (Fig. S10B, C). In isolated mitochondria, UFA content controlled the rate of respiration coupled to ADP-phosphorylation (State 3) and uncoupled (State 3u) from the PMF (Fig. 4B).

The role for diffusion in respiration provides a functional rationale for variations in lipids within and between cells. In eukaryotes, lipid species that increase membrane viscosity – sterols and sphingolipids – are depleted from energy-transducing membranes (*25*). In prokaryotes, analogous rigidifying lipids, such as hopanoids and archaeal ether lipids, are associated with niches where the robustness of the membrane as a permeability barrier is paramount over rapid metabolic activity (*26*). Such a trade-off is evident in *E. coli*, which eliminates lipid unsaturation through cyclopropanation during stationary phase to survive in acidic conditions (*27*). Localizing ETCs to fluid internal membranes while maintaining rigid outer membranes could thus have served as an advantage during the evolution of dedicated metabolic organelles. In some mitochondria, ETCs are additionally organized by supercomplexes of respiratory enzymes (*28*, *29*). In our simulations, tethering of DH and TO enzymes increased respiration rates and reduced anisotropy in the quinone pool (Fig. S11, Mov. S2, Supporting Text). A diffusion-coupled reaction model could thus be important for understanding how the interplay between lipid composition, enzymatic activity, and membrane organization dictates respiratory function in a wide range of systems.

References and Notes:

1. E. Muro, G. E. Atilla-Gokcumen, U. S. Eggert, Lipids in cell biology: how can we understand them better? *Mol. Biol. Cell*. **25**, 1819–1823 (2014).
2. T. Harayama, H. Riezman, Understanding the diversity of membrane lipid composition. *Nat. Rev. Mol. Cell Biol.* **19**, 281-96 (2018).
3. R. Covino *et al.*, A Eukaryotic Sensor for Membrane Lipid Saturation. *Mol. Cell*. **63**, 1–11 (2016).
4. M. Sinensky, Homeoviscous Adaptation--A Homeostatic Process That Regulates the Viscosity of Membrane Lipids in Escherichia coli. *Proc. Natl. Acad. Sci. U. S. A.* **71**, 522–525 (1974).
5. J. R. Hazel, Thermal Adaptation in Biological Membranes: Is Homeoviscous Adaptation the Explanation? *Annu. Rev. Physiol.* **57**, 19–42 (1995).

6. Y. Feng, J. E. Cronan, Escherichia coli Unsaturated Fatty Acid Synthesis: Complex transcription of the fabA gene and in vivo identification of the essential reaction catalyzed by FabB. *J. Biol. Chem.* **284**, 29526–29535 (2009).

7. A. Khlebnikov, K. A. Datsenko, T. Skaug, B. L. Wanner, J. D. Keasling, Homogeneous expression of the PBAD promoter in Escherichia coli by constitutive expression of the low-affinity high-capacity AraE transporter. *Microbiology*. **147**, 3241–3247 (2001).

8. M. A. Kay, C. He, Z. Chen, A robust system for production of minicircle DNA vectors. *Nat. Biotechnol.* **28**, 10–14 (2010).

9. J. E. Cronan, E. P. Gelman, An Estimate of the Minimum Amount of Unsaturated Acid Required for Growth of Escherichia coli. *J. Biol. Chem.* **248**, 1188–1195 (1973).

10. P. G. Saffman, M. Delbrock, Brownian motion in biological membranes. *Proc. Natl. Acad. Sci. U. S. A.* **72**, 3111–3113 (1975).

11. K. B. Andersent, K. Von Meyenburgt, Are Growth Rates of Escherichia coli in Batch Cultures Limited by Respiration? *J. Bacteriol.* **144**, 114–123 (1980).

12. A. N. Woodmansee, J. A. Imlay, Reduced flavins promote oxidative DNA damage in non-respiring Escherichia coli by delivering electrons to intracellular free iron. *J. Biol. Chem.* **277**, 34055–34066 (2002).

13. T. Yura, K. Nakahigashi, Regulation of the heat-shock response. *Curr. Opin. Microbiol.* **2** (1999), pp. 153–158.

14. A. C. Brouwer, J. F. Kirsch, Investigation of Diffusion-Limited Rates of Chymotrypsin Reactions by Viscosity Variation. *Biochemistry*. **21**, 1302–1307 (1982).

15. A. Kroger, Klingenb, Schweidl, Kinetics of Redox Reactions of Ubiquinone Related To Electron- Transport Activity in Respiratory Chain. *Eur. J. Biochem.* **34**, 358–368 (1973).

16. P. R. Rich, A generalised model for the equilibration of quinone pools with their biological donors and acceptors in membrane-bound Electron Transfer Chains. *FEBS Lett.* **130**, 173–178 (1981).

17. B. Chazotte, C. R. Hackenbrock, Lateral Diffusion as a Rate-limiting Step in Ubiquinone-mediated Mitochondrial Electron Transport. *J. Biol. Chem.* **264**, 4978–4985 (1989).

18. S. Gupte *et al.*, Relationship between lateral diffusion, collision frequency, and electron transfer of mitochondrial inner membrane oxidation- reduction components. *Proc. Natl. Acad. Sci. U. S. A.* **81**, 2606–2610 (1984).

19. C. Blanchi, M. L. Genova, G. P. Castelli, G. Lenaz, The mitochondrial respiratory chain is partially organized in a supercomplex assembly: Kinetic evidence using flux control analysis. *J. Biol. Chem.* **279**, 36562–36569 (2004).

20. R. Fato, M. Battino, M. D. Esposti, G. P. Castelli, G. Lenaz, Determination of Partition and Lateral Diffusion Coefficients of Ubiquinones by Fluorescence Quenching of n-(9-Anthroy1oxy)stearic Acids in Phospholipid Vesicles and Mitochondrial Membranes. *Biochemistry*. **25**, 3378–3390 (1986).

21. I. Llorente-Garcia *et al.*, Single-molecule in vivo imaging of bacterial respiratory complexes indicates delocalized oxidative phosphorylation. *Biochim. Biophys. Acta - Bioenerg.* **1837**, 811–824 (2014).

22. T. Lenn, M. C. Leake, C. W. Mullineaux, Clustering and dynamics of cytochrome bd-I complexes in the Escherichia coli plasma membrane in vivo. *Mol. Microbiol.* **70**, 1397–1407 (2008).

23. M. D. Brand, P. Couture, P. L. Else, K. W. Withers, A. J. Hulbert, Evolution of energy metabolism Proton permeability of the inner membrane of liver mitochondria is greater in a mammal than in a reptile. *Biochem. J.* **275**, 81–86 (1991).

24. M. J. Torres *et al.*, 17β-Estradiol Directly Lowers Mitochondrial Membrane Microviscosity and Improves Bioenergetic Function in Skeletal Muscle. *Cell Metab.* **27**, 167–179.e7 (2017).

25. G. van Meer, D. R. Voelker, G. W. Feigenson, Membrane lipids: where they are and how they behave. *Nat. Rev. Mol. Cell Biol.* **9**, 112–24 (2008).

26. D. L. Valentine, Adaptations to energy stress dictate the ecology and evolution of the Archaea. *Nat. Rev. Microbiol.* **5**, 316–23 (2007).

27. Y.-Y. Chang, J. E. Cronan, Membrane cyclopropane fatty acid content is a major factor in acid resistance of Escherichia coli. *Mol. Microbiol.* **33**, 249–259 (1999).

28. D. Milenkovic, J. N. Blaza, N. G. Larsson, J. Hirst, The Enigma of the Respiratory Chain Supercomplex. *Cell Metab.* **25**, 765–776 (2017).

29. J. A. Letts, K. Fiedorczuk, L. A. Sazanov, The architecture of respiratory supercomplexes. *Nature*. **537**, 644–648 (2016).

30. J. W. Campbell, J. E. C. Jr, Escherichia coli FadR Positively Regulates Transcription of the fabB Fatty Acid Biosynthetic Gene Escherichia coli FadR Positively Regulates Transcription of the fabB Fatty Acid Biosynthetic Gene. **183** (2001), doi:10.1128/JB.183.20.5982.

31. H. J. Cha Srivastava, R., Vakharia, V., Rao, G., and W. E. Bentley, Green fluorescent protein as a non-invasive “stress probe” in resting recombinant Escherichia coli culture. *Appl. Environ. Microbiol.* **65**, 409–414 (1999).

32. R. W. Haushalter *et al.*, Production of anteiso-branched fatty acids in Escherichia coli; next generation biofuels with improved cold-flow properties. *Metab. Eng.* **26C**, 111–118 (2014).

33. H. Alper, C. Fischer, E. Nevoigt, G. Stephanopoulos, *Proc. Natl. Acad. Sci. U. S. A.*, 102, 12678-83 (2005).

34. D. Degreif, T. de Rond, A. Bertl, J. D. Keasling, I. Budin, Lipid engineering reveals regulatory roles for membrane fluidity in yeast flocculation and oxygen-limited growth. *Metab. Eng.* **41**, 46–56 (2017).

35. R. Herzog *et al.*, Lipidxplorer: A software for consensual cross-platform lipidomics. *PLoS One*. **7**, 15–20 (2012).

36. M. Bekker *et al.*, Changes in the redox state and composition of the quinone pool of Escherichia coli during aerobic batch-culture growth. *Microbiology*. **153**, 1974–80 (2007).

37. T. S. Batth *et al.*, A targeted proteomics toolkit for high-throughput absolute quantification of Escherichia coli proteins. *Metab. Eng.* **26**, 48–56 (2014).

38. A. Kubalski, Generation of giant protoplasts of Escherichia coli and an inner-membrane anion selective conductance. *BBA - Biomembr.* **1238**, 177–182 (1995).

39. D. E. Koppel, M. P. Sheetz, M. Schindler, Lateral diffusion in biological membranes. A normal-mode analysis of diffusion on a spherical surface. *Biophys. J.* **30**, 187–92 (1980).

40. A. Milon *et al.*, Precise determination of the hydrodynamic radius of phospholipid vesicles near the phase transition. *Biochim. Biophys. Acta*. **777**, 331–333 (1984).

41. C. Burstein, L. Tiankova, A. Kepes, Respiratory control in Escherichia coli K 12. *Eur. J. Biochem.* **94**, 387–92 (1979).

42. V. B. Borisov *et al.*, Aerobic respiratory chain of Escherichia coli is not allowed to work in fully uncoupled mode. *Proc. Natl. Acad. Sci.* **108**, 17320–17324 (2011).

43. P. Munujos, J. Collcanti, F. Gonzalezsastre, F. J. Gella, Assay of Succinate Dehydrogenase Activity by a Colorimetric-Continuous Method Using Iodonitrotetrazolium Chloride as Electron Acceptor. *Anal. Biochem.* **212**, 506–509 (1993).

44. K. Matsushita, T. Ohnishi, H. R. Kaback, NADH-ubiquinone oxidoreductases of the Escherichia coli aerobic respiratory chain. *Biochemistry*. **26**, 7732–7737 (1987).

45. C. E. Vanorsdel *et al.*, The escherichia coli CydX protein is a member of the CydAB cytochrome bd oxidase complex and is required for cytochrome bd oxidase activity. *J. Bacteriol.* **195**, 3640–3650 (2013).

46. S. J. Koepke, J. J. Watkins, S. D. Minteer, Understanding the Role of Mitochondrial Health in the Mechanism of Mitochondrial Bioelectrocatalysis. *J. Electrochem. Soc.* **163**, H292–H298 (2016).

47. G. W. Rogers *et al.*, High throughput microplate respiratory measurements using minimal quantities of isolated mitochondria. *PLoS One*. **6,** e21746 (2011).

48. K. Kita, K. Konishi, Y. Anraku, Terminal Oxidases of Escherichia coli Aerobic Respiratory Chain I. *J. Biol. Chem.* **259**, 3368–3374 (1984).

49. D. Shoup, A. Szabo, Role of diffusion in ligand binding to macromolecules and cell-bound receptors. *Biophys. J.* **40**, 33–9 (1982).

50. H. C. Berg, E. M. Purcell, Physics of chemoreception. *Biophys. J.* **20**, 193–219 (1977).

51. J. Keizer, J. Ramirez, E. Peacock-López, The effect of diffusion on the binding of membrane-bound receptors to coated pits. *Biophys. J.* **47**, 79–87 (1985).

52. D. A. Lauffenburger, J. Linderman, *Receptors: models for binding, trafficking, and signaling* (Oxford University Press, 1993).

53. T. Althoff, D. J. Mills, J.-L. Popot, W. Kühlbrandt, Arrangement of electron transport chain components in bovine mitochondrial supercomplex I1III2IV1. *EMBO J.* **30**, 4652–64 (2011).

54. E. Lapuente-Brun *et al.*, Supercomplex assembly determines electron flux in the mitochondrial electron transport chain. *Science* **340**, 1567–70 (2013).

55. J. N. Blaza, R. Serreli, A. J. Y. Jones, K. Mohammed, J. Hirst, Kinetic evidence against partitioning of the ubiquinone pool and the catalytic relevance of respiratory-chain supercomplexes. *Proc. Natl. Acad. Sci. U. S. A.* **111**, 15735–40 (2014).

56. N. Oppenheimer, H. A. Stone, Effect of Hydrodynamic Interactions on Reaction Rates in Membranes. *Biophys. J.* **113**, 440–447 (2017).

57. D. Marchal, W. Boireau, J. M. Laval, J. Moiroux, C. Bourdillon, Electrochemical measurement of lateral diffusion coefficients of ubiquinones and plastoquinones of various isoprenoid chain lengths incorporated in model bilayers. *Biophys. J.* **74**, 1937–48 (1998).

58. I. Llorente-Garcia *et al.*, Single-molecule in vivo imaging of bacterial respiratory complexes indicates delocalized oxidative phosphorylation. *Biochim. Biophys. Acta - Bioenerg.* **1837**, 811–824 (2014).

59. A. Nenninger *et al.*, Independent mobility of proteins and lipids in the plasma membrane of Escherichia coli. *Mol. Microbiol.* **92**, 1142–1153 (2014).

60. R. Peters, R. J. Cherry, Lateral and rotational diffusion of bacteriorhodopsin in lipid bilayers: experimental test of the Saffman-Delbrück equations. *Proc. Natl. Acad. Sci. U. S. A.* **79**, 4317–4321 (1982).

61. P. Cicuta, S. L. Keller, S. L. Veatch, Diffusion of liquid domains in lipid bilayer membranes. *J. Phys. Chem. B*. **111**, 3328–3331 (2007).

62. Y. Gambin *et al.*, Lateral mobility of proteins in liquid membranes revisited. *Proc. Natl. Acad. Sci.* **103**, 2098–2102 (2006).

63. N. A. Newton, G. B. Cox, F. Gibson, Function of ubiquinone in Escherichia coli: a mutant strain forming a low level of ubiquinone. *J. Bacteriol.* **109**, 69–73 (1972).

64. K. Kita, K. Konishi, Y. Anraku, Terminal Oxidases of Escherichia coli Aerobic Respiratory Chain II. *J. Biol. Chem.* **259**, 3368–3374 (1984).

65. M. Braun, S. Bungert, T. Friedrich, Characterization of the overproduced NADH dehydrogenase fragment of the NADH:ubiquinone oxidoreductase (complex I) from Escherichia coli. *Biochemistry*. **37**, 1861–1867 (1998).

66. K. Bjorklof, V. Zickermann, M. Finel, Purification of the 45 kDa, membrane bound NADH dehydrogenase of Escherichia coli (NDH-2) and analysis of its interaction with ubiquinone analogues. *FEBS Lett.* **467**, 105–110 (2000).

67. E. Maklashina *et al.*, Fumarate reductase and succinate oxidase activity of Escherichia coli complex II homologs are perturbed differently by mutation of the flavin binding domain. *J. Biol. Chem.* **281**, 11357–11365 (2006).

68. M. Bekker *et al.*, Changes in the redox state and composition of the quinone pool of Escherichia coli during aerobic batch-culture growth. *Microbiology*. **153**, 1974–1980 (2007).

69. V. Sharma *et al.*, Panorama: A targeted proteomics knowledge base. *J. Proteome Res.* **13**, 4205–4210 (2014).

70. J. Suurkuusk, B. R. Lentz, Y. Barenholz, R. L. Biltonen, T. E. Thompson, A Calorimetric and Fluorescent Probe Study of the Gel-Liquid Crystalline Phase Transition in Small, Single-Lamellar Dipalmitoylphosphatidylcholine Vesicles. *Biochemistry*. **15**, 1393–1401 (1976).

Acknowledgments: Naomi Oppenheimer, Howard Stone, and Dan Arlow contributed helpful discussions and the Coates (University of California, Berkley) and Lippincott-Schwartz (Janelia Research Campus) labs contributed experimental assistance. **Funding:** This work was part of the DOE Joint BioEnergy Institute supported by the U. S. Department of Energy, Office of Science, Office of Biological and Environmental Research, through contract DE-AC02-05CH11231 between Lawrence Berkeley National Laboratory and the U. S. Department of Energy. This work was also supported by National Science Foundation grants MCB-1442724 and MCB-1715681 to J.D.K, and a Junior Fellowship to I.B. from the Miller Institute for Basic Research. **Author contributions:** I.B. designed the study and performed the experiments. T.d.R. developed the model with I.B. and performed chemical synthesis. Y.C., LJ.G.C., and C.J.P. performed protein mass spectrometry analysis. All authors wrote the paper and discussed the results. **Competing interests:** J.D.K. has a financial interest in Amyris, Lygos, Demetrix, Constructive Biology, Maple Bio, and Napigen. The research described in this publication is not related to the work of these companies. **Data and material availability:** All strains are available from the Joint BioEnergy Institute public registry (http://public-registry.jbei.org). Protein mass spectrometry SRM data and methods are available at Panamoramaweb (http://goo.gl/JJySak). The ETC simulation script, written in Python, as well as examples of commands to invoke it, are available at GitHub (http://github.com/tderond/Budin2018).

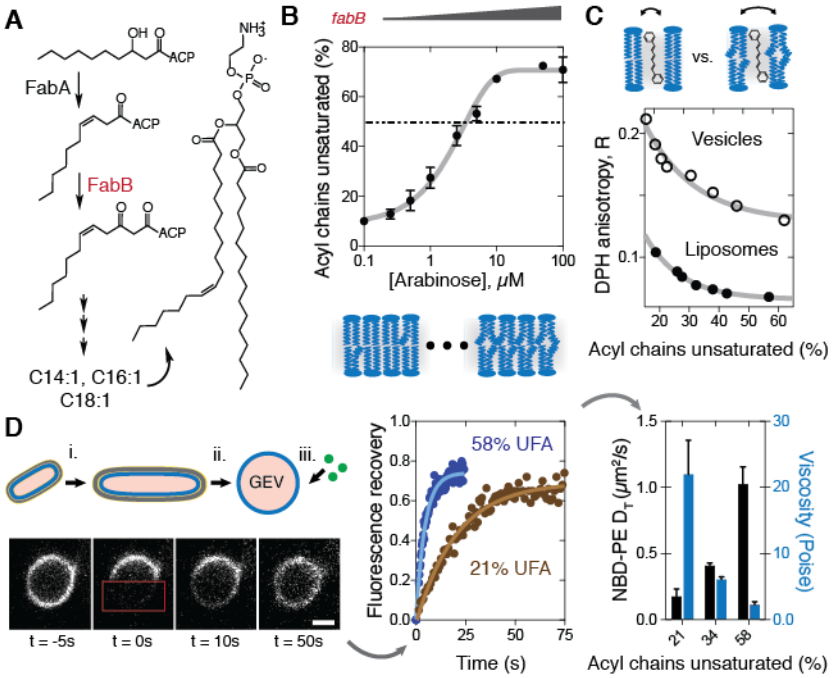

Fig. 1. Genetic titration of inner membrane viscosity in *E. coli*. (**A**) The pathway for bacterial UFA synthesis. The activity of FabB is rate-limiting for UFA synthesis and incorporation into phospholipids. (**B**) Titration of *fabB* expression with the P_{BAD} promoter modulates UFA stoichiometry as a function of inducer (arabinose) concentration. This leads to membranes with increasing amounts of *cis* double bonds, as shown in the model. Data are mean +/- SD ($N = 3$). (**C**) Characterization of membrane ordering using DPH anisotropy. Higher anisotropy values indicate restricted motion of the probe and therefore a more ordered membrane. (**D**) A FRAP-based assay for measuring inner membrane diffusivities and its application in estimating membrane microviscosity. GEVs were generated by elongating cells with cephalexin (*i*). Cell walls were then digested (*ii*), thereby generating large, inner membrane vesicles to which lipid fluorophores can be added externally (*iii*). Shown is an experiment for a model substrate, NBD-PE, with recovery curves for two lipid compositions. Translational diffusion coefficients (D_T) were generated from the exponential constant of the recovery curve and viscosity values were then estimated from these. Black bars show the calculated diffusion coefficients for NBD-PE (left Y-axis), and blue bars show the extrapolated estimated membrane viscosity (right Y-axis). Data are mean +/- SEM ($N = 5$).

(2 columns)

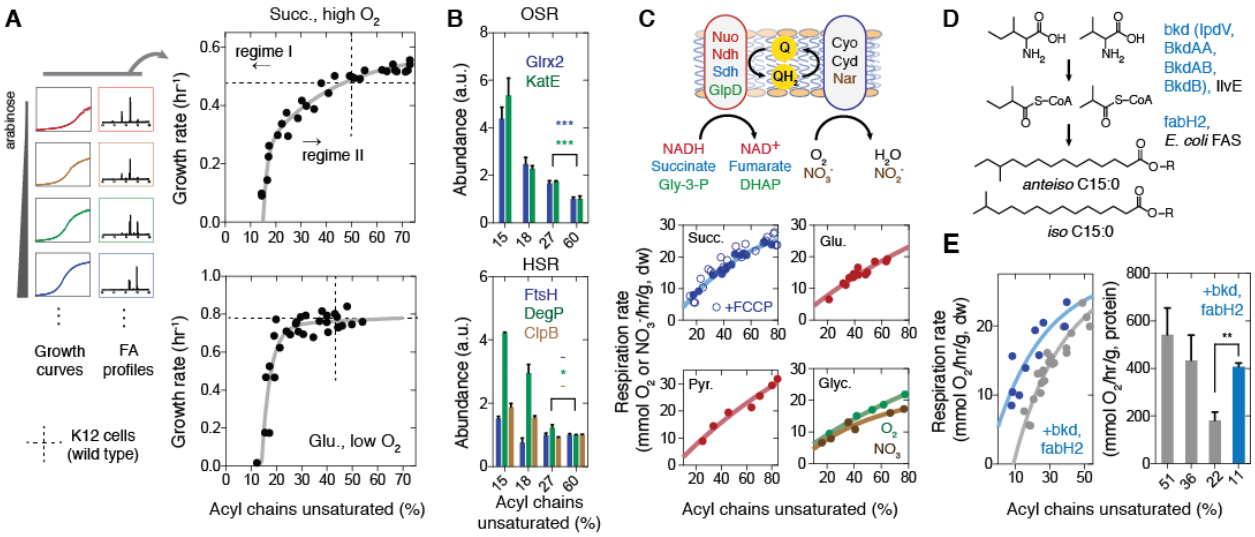

Fig. 2. Effects of fatty acid composition on physiology and respiratory metabolism. (**A**) Growth rates and FA compositions were characterized for a series of batch cultures with various arabinose concentrations. The growth rate dependence on UFA levels occurs in two phases: a fitness cliff at low levels (regime I), and a gradual increase in growth rates at intermediate levels (regime II); these can be described by two exponential constants: $k_1 \sim 0.6\ \%^{-1}$, $k_2 \sim 0.03\ \%^{-1}$ at 37 °C. The top plot shows the growth rate dependence under respiratory conditions (succinate, high oxygen) while the bottom shows it for fermentative conditions (glucose, low oxygen), when regime II is absent. (**B**) Abundance of stress response factors in response to different proportions of unsaturated acyl chains. Data are mean +/- SEM ($N = 3$) and overlaid are the results of t-tests for significance between abundances in high (60%) and intermediate (27%) lipid unsaturation. ***, $p < 0.001$; *, $p < 0.05$, -, no significance. (**C**) The modular *E. coli* ETC consists of dehydrogenase (red) and terminal oxidase (blue) enzymes that react via an intermediate quinone pool. The different enzyme complexes utilized are color coded according to substrate. The corresponding respiration rates, as measured by oxygen or nitrate consumption, show a similar dependence ($k \sim 0.01\text{-}0.03\ \%^{-1}$) on lipid unsaturation regardless of the electron donor or acceptor and whether the ETC is uncoupled by FCCP. (**D**) Heterologous biosynthesis of *anteiso* and *iso* BCFAs from amino acid precursors in *E. coli* using genes (highlighted in blue) from *B. subtilis*. (**E**) Effects of BCFA biosynthesis on uncoupled succinate respiration rates with various levels of lipid unsaturation (left). In purified membrane vesicles (right), the abundance of unsaturated fatty acids also mediates succinate respiration and a UFA deficiency can be rescued by BCFA biosynthesis, which increases respiration rates in UFA-depleted membranes (t-test for significance $p = 0.002$, **). Data are mean +/- SEM ($N = 3$).

(3 columns)

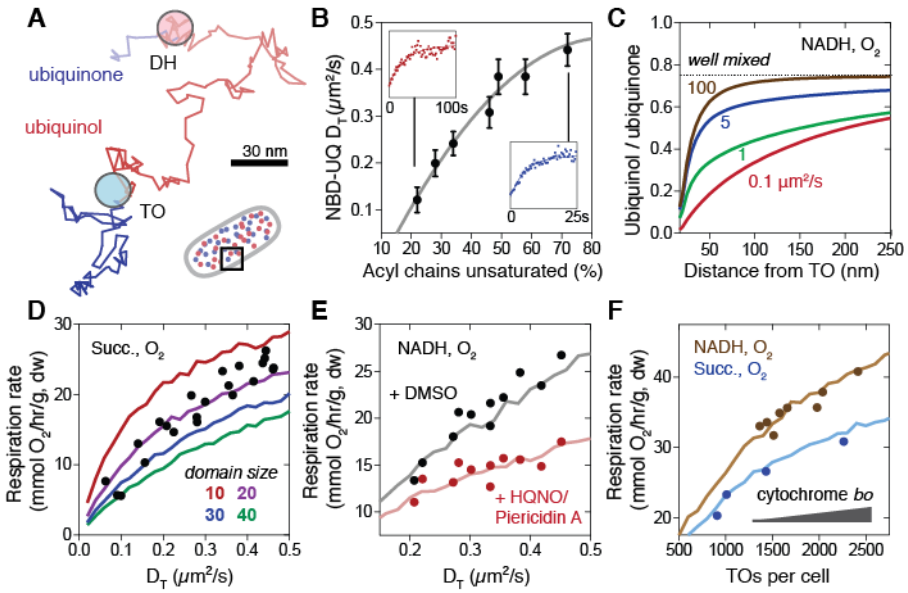

Fig. 3. Testing a diffusion-coupled reaction model for bacterial respiration. (**A**) A simulated random walk by a ubiquinone, which becomes reduced (ubiquinol, red) upon interaction with a DH domain and then oxidized (blue) upon subsequent collisions with a TO, an oxygen consuming reaction. The opacity of the path indicates progression during the time course (100 ms). (**B**) Experimental measurements of ubiquinone diffusivity in GEVs. Values are shown as averages from eight GEVs for each preparation. Solid line shows a quadratic function fit to the data, and is used as a standard curve to convert lipid composition to diffusivity in subsequent experiments. Inserts show example FRAP exponential recovery curves. Data are mean +/- SEM (N =5). (**C**) The distribution of the ubiquinone pool as a function of its diffusivity in whole cell simulations, expressed as the steady-state average ubiquinol:ubiquinone ratio within a given radius of a TO. (**D**) Comparison of the simulated dependence of ubiquinone diffusivity (D_T) on respiration rates (solid lines) with measurements of uncoupled respiration in succinate medium (dots). Values in the legend are the domain size of the modeled ETC enzyme pair. (**E**) Modeling the effect of reducing enzymatic activity using the inhibitors N-oxo-2-heptyl-4-hydroxyquinoline (HQNO) and piericidin A, which act on TOs and NADH DH, respectively. Simulated rates of NADH-linked respiration (solid lines), modeled using 20-mer homotypic domains, are shown alongside uncoupled respiration rates in pyruvate medium (dots) under various UFA levels with HQNO (20 µM) and Piericidin A (100 nM), or with no inhibitors (DMSO). (**F**) The effect of changes in TO concentration – achieved by titrating expression of *cyoABCD* – on respiratory rates. Simulation results (solid lines) are superimposed with experimental measurements of NADH respiration with pyruvate (brown) and succinate respiration (blue); measured TO abundance includes both aerobic cytochrome oxidases (*bo* and *bd*-I).

(2 columns)

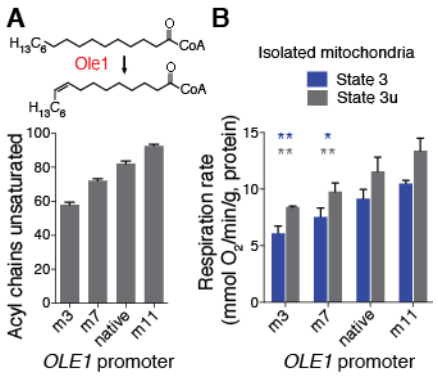

Fig. 4. Lipid-mediated respiration in mitochondria. (**A**) The desaturase Ole1 generates all UFAs in yeast. Unsaturated lipid composition is controlled by the promoter driving expression of *OLE1* - either the native one, or one of three variants (m3, m7, m11) in engineered strains. (**B**) Mitochondrial respiration rates in coupled (State 3, 0.5 mM ADP) and uncoupled (State 3u, 4 µM FCCP) conditions corresponded with unsaturated lipid content. Mitochondria were incubated with 5 mM succinate as a substrate. Data are mean +/- SEM ($N = 3$) and overlaid are the results of t-tests for significance against m11. **, $p < 0.01$; *, $p < 0.05$.

(1 column)

Supplementary Materials:

Materials and Methods

Figures S1-S11

Tables S1-S3

Movies S1-S2

References (*30-70*)

Supplementary Materials for

Viscous control of cellular respiration by membrane lipid composition

Itay Budin, Tristan de Rond, Yan Chen, Leanne Jade G. Chan, Christopher J. Petzold, and Jay D. Keasling

correspondence to: keasling@berkeley.edu, budin@berkeley.edu

This PDF file includes:

Other Supplementary Materials for this manuscript includes the following:

Materials and Methods

Strain engineering and cloning

Wild-type K12 (MG1655, *E. coli* Genetic Stock Resource Center) and the arabinose titratable strain BW27783-2T (*8*) were used as base strains in this study. The deletion of *fabB* was performed as previously described (*30*) and was maintained on media containing oleic acid. Deletion of *fabR* in MG1655 was performed via P1 phage transduction from the corresponding Keio strain. Deletion of *cyoABCD* was performed in BW27783 by homologous recombination of an in-frame *kanR* via the lambda red method.

For plasmid construction, UFA synthesis genes *fabA* and *fabB* were amplified from MG1655 genomic DNA and inserted into PBAD30 (p15a origin, AmpR) using ligation cloning with SD sequences encoded in the amplification primers. Plasmids for expressing *cyoABCD* were similarly cloned with a range of SD sequences into the P_{BAD} plasmid pBbA1a (p15a origin, AmpR). For the heat shock promoter assay, the promoter of *clpB* was amplified as previously described (*31*) from MG1655 genomic DNA and was used to replace the *lacUV5* promoter driving GFP expression in pBbB2k-GFP. For BCFA synthesis, *fabH2* and the *bkd* operon of *B. subtilis* were amplified from pIlvC.bfabH2 and pPhatty.Bkd (*32*), provided by Dr. Robert Haushalter, and introduced as a single operon into pBbB5k (BBR1 origin, KanR) connected by a strong RBS proceeding *fabH2*. The gene cassette for AcrAB-GFP was provided by Dr. Heather Jenson and was cloned into pBbB5k using Gibson assembly.

For *OLE1* promoter substitution in *S. cerevisiae*, a set of constitutive TEF1 promoter mutants that have previously been generated (*33*) was utilized. Promoter substitution of the native *OLE1* promoter was performed as previously described (*34*).

Cell growth

Bacteria were grown in MOPS minimal medium (Teknova) pH 7.4 supplemented with 0.6% w/v of the given carbon source. Inducer was added to media before cells for continuous induction. Experiments were generally carried out by growing a pre-culture directly from glycerol stock for 24-36 hours in media supplanted with antibiotics and oleic acid. Cells were then centrifuged, washed, and diluted into growth cultures lacking lipid supplement and antibiotic, but with given inducer concentrations. For BCFA experiments, cells were diluted into minimal media supplemented with amino acids (Teknova 5X EZ Rich supplement), which supplied abundant branched chain amino acid precursors for BCFA synthesis

For growth rate analysis, OD600 values were recorded for 1 mL culture volumes in clear 24-well plates (Flacon) sealed with gas permeable adhesive film (Thermo Fisher Scientific) on a Synergy 4 plate reader (Biotek) under high speed shaking. Microaerobic growth curves were carried out similarly but with slow speed shaking. During runs, cells were sampled (0.25 mL) during exponential phase for lipid analysis. For all other experiments, cells were grown in 25- or 50-mL volumes in 250-mL shake flasks, which yielded similar growth rates (Fig. S4A). Unless otherwise noted, cells were sampled during mid-log phase at OD ~ 0.4; OD values were converted to dry cell weight using a strain-specific standard curve.

Yeast cells were grown in 25-50 mL volumes in 250-mL shake flasks in YPD or complete synthetic media with 2% glucose as the carbon source. For harvesting mitochondria, cells were grown for 36 hours in order to be in a respiratory state.

Chemical analyses

Total *E. coli* lipids were extracted using a modified Bligh-Dyer method by adding a resuspended cell pellet (in 100 µL of water) into 2 mL of 1:1 chloroform:methanol. Following vigorous vortexing and the addition of 1 mL of water, the organic layer was extracted and dried in glass tubes. For GC-MS analysis, fatty acid methyl esters (FAMEs) were prepared by solubilizing dried lipid extracts in 200 µL toluene followed by addition of 1.5 mL of sodium methoxide in methanol. After incubation for 20 min at 55º, 300 µL of hexane and 1 mL of water were added and FAMEs were extracted from the organic, hexane layer. Samples were run on a Agilent 5973 GC-MS using a 30 meter DB-5ms capillary column and analyzed as previously described (*34*). For samples with BCFAs, FAMEs were generally run under a longer temperature gradient (10º/min until 300º), with species identification performed by fragmentation pattern analysis and quantification with the 55 molecular ion. Yeast fatty acids were analyzed as previously described (*34*).

Polar lipid analysis was performed using a shotgun lipidomics platform through a commercial service (LipoType GmbH). For this analysis, cells were grown under one of three inducer concentrations (0.25, 2, and 10 µM arabinose) in triplicate. Lipids from frozen pellets (10 mg dry weight) were extracted using chloroform:methanol, combined with internal lipid standards, and injected into a QExactive mass spectrometer (Thermo Scientific) equipped with a TriVersa NanoMate ion source (Advion Biosciences). Data was processed and analyzed using software based on LipoXplorer (*35*).

Fermentation products were analyzed by an HPLC system (Agilent 1100 Series) equipped with a refractive index detector (Agilent 1200 Series) and an ion-exclusion column (Aminex HPX-87H, Bio-Rad). After 24 hours of microaerobic growth on glucose, aliquots of supernatant were filtered through a 0.45 µm membrane and eluted through the HPLC column at 5ºC with 4 mM sulfuric acid at 0.6 mL/min for 25 min. Organic acids were quantified using external standards. HPLC was also used to quantifying quinone content of cells for the respiration model. Ubiquinone-8 was extracted from 20 mL of exponentially growing (OD ~ 0.4) cells in succinate media and analyzed as previously described (*36*) on an Eclipse XD8 C18 column (Agilent) an HPLC system (Agilent 1100 Series) with a diode-array detector. Concentration was measured by 260 nm absorbance and quantified using ubiquinone-10 (Sigma) as an external standard.

Proteomics

Factors upregulated during changes in lipid unsaturation were first identified by shotgun proteomics of cells grown under four different arabinose concentrations (0.1, 0.5, 1.0, 10) in triplicate (data not shown). Upregulated factors were then chosen for quantification by selected reaction monitoring (SRM) mass spectrometry as previously described (*37*). For ETC modeling, abundances of aerobic ETC enzymes (Sdh, the NADH DHs Ndh and Nuo, and the cytochrome oxidases Cyd and Cyo) were quantified using custom-synthesized peptide standards (Genscript). For each protein, three peptides were designed from previous shotgun proteomic data and assayed. Of these, the most linearly responsive peptide from each protein (Table S3) was chosen to quantify from. Further details of this analysis are in the Supplementary Text.

Biophysical analyses

For DPH anisotropy, liposomes were prepared by rehydrating extracted *E. coli* lipids from 50 mL of exponentially growing cells in buffer (10 mM HEPES pH 7.4) under tumbling at 37ºC overnight. Membrane vesicles were generated by 30 minutes of lysozyme treatment of exponentially growing cells (0.1 mg/mL in 100 mM Tris pH 7.2 with 10 mM EDTA).

Spheroplasts were then centrifuged (5000g, 10 minutes), resuspended in 100 mM HEPES pH 7.4, and disrupted via tip sonication (2 minutes in 15s pulses). Membrane vesicles were then isolated by ultracentrifugation (120,000g, 30 minutes) and resuspended in 1 mL of fresh buffer. DPH was added to both liposomes and membrane vesicles as a concentrated solution in ethanol and steady state fluorescence anisotropy was measured as previously described (*34*).

For diffusivity measurements, giant *E. coli* spheroplasts were generated as previously described (*38*) with modifications. Exponential phase cells (OD ~ 0.2) were grown for an additional 2 doublings with 30 μg/mL of the division-inhibiting antibiotic cephalexin (Sigma), thereby generating elongated ('giant') cells. These cells were resuspended in osmotic buffer (0.8 M sucrose) and treated with lysozyme (0.1 mg/mL with 10 mM EDTA). The resulting inner membrane spheroplasts, generally 2-5 μm in diameter, were centrifuged (5000g, 10 min), gently resuspended in 0.7 M sucrose, and stored at -20ºC until needed. For FRAP experiments, GEVs were labeled with fluorescent substrate, NBD-PE (Invitrogen) or NBD-UQ. The synthesis and NMR characterization of NBD-UQ is detailed in the Supplementary Text. The NBD conjugates were dissolved in ethanol as concentrated (1 mM) stocks, which were added to the GEVs via rapid addition (1% v/v) under vortexing, followed by incubation at room temperature for 30 minutes. In the case of NBD-UQ, co-addition with 1% BSA improved labeling efficiency. Labeled GEVs were imaged on a Zeiss LSM 710 confocal microscope whose stage was maintained at 37ºC using a forced-air stage heater (ASI 400, Nevtek). Bleaching experiments were carried about using the same 488 nm laser used for imaging, but with maximum laser power and long scanning time (~2 s). Bleaching through the GEV in the region of interest (azimuthal symmetry) by this method was confirmed by post-bleaching z-stacks. Images were acquired using ZEN software (Zeiss) and analyzed using ImageJ. Recovery after photobleaching was quantified as the ratio of intensity at the bleached edge compared to unbleached edge in the mid-plane of the GEV. Diffusion coefficients (D_T) were calculated from the exponential recovery curve using the fitted rate constant (*39*):

$$\mu_1(t) = \propto 1 - e^{-2tD_T/r^2}$$

where $\mu_1(t)$ is the normalized fluorescence intensity of the bleached edge and r is the radius of the GEV. Estimated membrane viscosities were calculated from diffusion coefficients by numerically solving the Saffman-Delbrück approximation (*10*) with finite viscosities:

$$D_T = \frac{1}{\eta_m}\left(\frac{k_B T}{4\pi h}\right)\left(ln\left(\frac{\eta_m h}{\eta_f a}\right) - \gamma\right)$$

where η_m and η_f are the viscosities of the membrane and external fluid (~0.01 Poise), respectively, k_B is Boltzmann's constant, T is temperature in Kelvin (310º), h is the thickness of the bilayer (~4 nm), a is the radius of the embedded protein or lipid [0.4 nm for NBD-PE (*40*)], and γ is Euler's constant.

Membrane imaging of live *E. coli* cells was carried out using phase contrast and epifluorescence imaging on a Leica DM6B microscope equipped with a CTO6 LED lamp and Hammamatsu C11440 camera. For fluorescence micrographs, cells carrying pBbB5k-AcrAB-GFP, expressing a reporter membrane protein, were grown under continual induction in 10 μM IPTG and then stained with the lipid dye FM4-64 (Invitrogen) at a concentration of 10 μM for 30 minutes at room temperature. For morphology quantification, a series of phase contrast images

were taken, and cell lengths were measured individually using LASX (Leica). For mitochondrial characterization, yeast cells were grown with a plasmid (PW1882) expressing a mitochondrial-targeted RFP and stained with Calcofluor-white (Sigma). Confocal z-stacks were acquired on Zeiss LSM 880 microscope; image acquisition, processing, and 3D reconstructions were performed using ZEN software.

Respiration measurements

For growing cells, oxygen consumption rates were recorded with a Clarke electrode (YSI) or in a Respiration Activity Monitoring System (RAMOS) (Khüner), which continuously monitors oxygen transfer. In RAMOS experiments, rates were normalized by OD and cell dry mass by taking samples at least two time points during exponential phase (OD 0.2 – 0.7). RAMOS experiments were also utilized to measure carbon dioxide production rates during yeast fermentation. For uncoupled bacterial respiration rates, measurements were taken in washed cells that were incubated without substrate, thereby allowing for respiratory control (*41*). For this, cells were spun and washed with carbon source-free media, and incubated for 30 minutes. Oxygen consumption was then measured with a microtiter-based time-resolved fluorescence assay (Extracellular Oxygen Consumption Assay, Abcam). Cells were added to individual wells on a 96-well plate preloaded with reporter dye, fresh MOPS and carbon source, uncoupler (3 μM FCCP, added in DMSO) and sealed with mineral oil. Continuous readings were taken with time resolved fluorescence at 652 nm (excitation 380 nm, 30 μs lag time, 100 μs gate time) on a Synergy 4 plate reader (Biotek) incubated at 37ºC. Samples were measured in technical triplicate, whose average maximum rate of fluorescence increase was used. The increase (slope) in time resolved fluorescence was converted to oxygen consumption rates by simultaneous measurement of glucose oxidase standards (0.1-1 μ/mL), whose absolute respiration rates were previously measured on a Clarke electrode (YSI). This approach allowed for multiplexed respiratory measurements with technical replicates and in smaller volumes compared to using a Clarke electrode directly. For inhibition experiments, HQNO (Abcam) and Piericidin A (Cayman Chemical) were added at 20 μM and 200 nM, respectively, as 100x stocks in DMSO. These concentrations corresponded to the approximate IC_{50} for cytochrome oxidase and NADH dehydrogenase activities.

Anaerobic respiration rates were measured by nitrate and nitrite measurements of supernatant from cells grown in sealed flasks initially purged with nitrogen. Anaerobic medium (MOPS 0.6% glycerol) contained 10 mM sodium nitrate to serve as an alternative electron acceptor. Samples were taken through a purged syringe and filtered before analysis. Nitrate and nitrite concentrations were measured with ion chromatography (Dionex ICS-1500) and quantified using standards. Maximum nitrate consumption during exponential growth (OD 0.2 – 0.4) was used to quantify respiration, since nitrite simultaneously underwent further oxidation.

For respiration in isolated membranes, inside-out vesicles were prepared from 50 mL of exponentially growing cells as previously described (*42*) with minor modifications. For membrane disruption, a cup-horn sonicator (Qsonic Q700 with 431MPX horn) was used at max amplitude for one hour, with 1 min on, 1 min off cycle, in a refrigerated (3-7 ºC) circulating bath. Compared to standard tip sonication, this method provided vesicles with more consistent intactness (assayed by their respiratory control) across lipid composition. After disruption and isolation by ultracentrifugation (120,000g, 30 minutes), membrane vesicles were resuspended in buffer (25 mM Bis-Tris Propane pH 7.5) and their abundance was quantified by their protein content using a BSA assay (Pierce). Respiration of inside-out-vesicles was measured using time

the fluorescence oxygen consumption assay, as described above, with vesicles (10 µg protein) in the presence of 10 mM sodium succinate, 10 mM $MgSO_4$, and 1 µM FCCP.

Isolated ETC enzyme activities were measured using published protocols: succinate dehydrogenase activity in washed cells using a colorimetric assay based on the reduction of INT (iodonitrotetrazolium) (*43*), NADH dehydrogenase activity in membrane vesicles using DCIP (2,6-Dichlorophenolindophenol) as a soluble acceptor (*44*), and cytochrome oxidase activity in membrane vesicles using the soluble electron donor TMPD (*N,N,N',N'*-tetramethyl-*p*-phenylenediamine) (*45*).

Mitochondrial respiration was analyzed on a Seahorse XFe96 Analyzer (Agilent) as previously described (*46*, *47*). Mitochondria were isolated from spheroplasted yeast cells by centrifugation using a commercial kit (Abcam) and quantified by total protein content using a BSA assay (Pierce).

Modeling

Brownian motion and collision-coupled reactions of electron carriers and ETC enzymes was modeled using a Wiener process using parameters that were either experimentally measured or taken from literature. Whole cell simulations (5000 steps, 0.5 ms step times) were carried out with a Python/NumPy script and run on the Joint BioEnergy Institute computing cluster. Each experimental condition was run in quintuplicate, with rates averaged over the last 2500 steps, in order to approximate a steady state. Further details and discussion of the diffusion-coupled reaction model are found in the Supplementary Text.

Supplementary Text

Model for diffusion-coupled respiration

A. Background and overview

In principle, the viscosity of a biological membrane would control the diffusion and interactions of components (proteins, lipids) embedded or associated with the bilayer. If these interactions are rate-limiting for a reaction process, then viscosity could control reactivity (diffusion-controlled reactions). In bulk aqueous solution, diffusion-controlled reactions are generally associated with fast enzymes, whose k_{cat}/K_M is on the order of 10^8 to 10^9 s^{-1}/M. Lipid membranes feature viscosities which are at least 100-fold higher than aqueous solutions, and so enzyme diffusion limits would drop accordingly. Purified respiratory enzymes from *E. coli* exhibit activities close to or within this range – e.g. a k_{cat}/K_M $5x10^6$ for cytochrome *bo* (*48*) – suggesting that diffusion plays a significant role in bacterial ETCs.

Analytical solutions have been developed for evaluating rates of diffusion-coupled reactions on cell surfaces (*49–51*). As worked out by Lauffenburger and Linderman (*52*), the coupling reaction rate (k_c) can be derived as a function of the diffusive transport rate (k_+) and the reaction rate constant (k_{on}):

$$k_c = \left(\frac{1}{k_+} + \frac{1}{k_{on}}\right)^{-1} \quad (2)$$

So that when the diffusion rate is slow or the coupling rate is fast (e.g. an enzyme with a high k_{cat}), k_c converges to k_+ and the reaction is diffusion-limited. While most aqueous enzymatic

reactions are too slow to be diffusion-limited, the comparatively higher viscosity of lipid bilayers suggests that reactions within cell membranes are commonly so (*52*). The diffusive transport rate in two dimensions (Figure 3, bottom) can be derived by modeling the two membrane species (e.g. receptor and ligand) as randomly distributed points on a plane with effective encounter distance (s) – the distance at which reactions occur, which can be approximated, for example, as the radius of the enzyme. In this case, the diffusive transport rate can be expressed as:

$$k_+ = \frac{2\pi D_T}{\ln(b/s)} \tag{3}$$

Where D_T is the sum of the translational diffusion coefficients of the two species and b is a length term describing the average distance between interacting partners, which is concentration dependent. Notably, in this form, k_+ is in units of m^2/s, but it can be converted to those ($M^{-1}s^{-1}$) for a bimolecular on rate (k_{on}) by multiplying by Avogrado's number for molarity and by the thickness of the membrane for local volume.

When one of the interacting species diffuses faster (e.g. is smaller), D_T converges to its individual diffusivity. Therefore, in a simplified system with a single enzyme and small-molecule substrate, the net reaction rate of a diffusion-coupled reaction (k_c) is expected to scale linearly with the diffusivity of the substrate.

The diffusional distance term (b) in Eq. 3 is critical in determining the diffusion coupled reaction rate and the relative contribution of k_+ to k_c. Generally, this parameter can be estimated using the concentration and total membrane area if assuming an isotropic distribution of substrate. When considering ubiquinone-complex interactions in the ETC as simple single diffusion coupled reactions, however, b becomes exceedingly small due to the very high ubiquinone concentration in the cell (~2% of all lipids in the inner membrane of *E. coli*). However, substrate distribution is more complicated in the case of a dual reaction model that includes the activities of both oxidases and reductases on a shared quinone pool, as the bulk substrate concentration is dependent on the activity of each enzyme type. In addition, in a diffusion-limited reaction, local substrate concentrations are expected to become depleted compared to the bulk, and therefore average distances between particles cannot be calculated based on an isotropic distribution. Therefore, the simplified solutions outlined above for diffusion coupled reactions are not straightforward to carry out in this case, motivating an alternative approach for describing the system.

Numerical simulations have the advantage of considering important stochastic variations in parameters, such as the distribution of enzymes on a cell surface. In such stochastic models, Brownian motion is described as a Weiner process, in which displacements during each timestamp are independent random variables described by a Gaussian distribution with a mean (μ) of zero and dependent on the diffusion coefficient. For 2D diffusion, motion in x and y are computed independently and can be described as follows:

$$x(t_n + \Delta t) - x(t_n) = \mathcal{N}(\mu, \sigma^2) = \mathcal{N}(0, 2\Delta t * D_t) \tag{4}$$

$$y(t_n + \Delta t) - y(t_n) = \mathcal{N}(\mu, \sigma^2) = \mathcal{N}(0, 2\Delta t * D_t) \tag{5}$$

After the movement of all particles at each step, A reaction is then considered if there is collision between enzyme and substrate, defined by a ubiquinone/ubiquinol being within a defined distance (r) of the appropriate enzyme (see below). For each ubiquinone/ubiquinol

within an enzyme's radius, the probability of reacting is $P_{rxn} = k_{cat} * \Delta t$ (Δt is set such that $P_{rxn} \leq 1$). The model therefore considers both enzyme activities and diffusional interactions as defined by input parameters. To prevent them from taking up the same space, enzymes that have overlapping radii *r* (i.e. have a distance of less than 2*r*) are repelled from each other after applying Brownian motion, but before testing for enzymatic reactions, at each step.

An additional advantage of using a numerical model is that parameters can be elaborated upon to better mimic biological systems. For example, this model provides a simple way to analyze the diffusional effects of ETC supercomplexes, in which individual ETC enzymes bind to one or more of a different type, e.g. DH/TO heterodimers. These have been observed to a play role in mitochondrial respiration (*53*, *54*). One potential function, among several others (*28*), of such complexes would be to reduce the average diffusion distance that electron carriers must undergo in order to undergo a reaction in the absence of any sort of substrate channeling, which is unlikely based on the pool behavior of ubiquinone (*55*) and observed structural features of mammalian supercomplexes.

To simulate enzyme tethering in our model, we included code for tethering individual enzymes or enzyme domains of opposite types (i.e. a DH and TO) during simulations. Each enzyme is first assigned a partner. These two enzymes (*A* and *B*) then move towards each other up to an "ideal" distance l between them, at a rate proportional (the coefficient of proportionality being k) to the distance between the pair $|AB|$ minus l.

$$x_A(t_n + \Delta t) - x_A(t_n) = k\frac{x_B(t_n) - x_A(t_n)}{2|AB|}(|AB| - l) \quad (6)$$

$$y_A(t_n + \Delta t) - y_A(t_n) = k\frac{y_B(t_n) - y_A(t_n)}{2|AB|}(|AB| - l) \quad (7)$$

$$x_B(t_n + \Delta t) - x_B(t_n) = k\frac{x_A(t_n) - x_B(t_n)}{2|AB|}(|AB| - l) \quad (8)$$

$$y_B(t_n + \Delta t) - y_B(t_n) = k\frac{y_A(t_n) - y_B(t_n)}{2|AB|}(|AB| - l) \quad (9)$$

Due to wrapping of the field, the distance $|AB|$ used is the shortest found for all possible tessellations. In our simulations, *k* was 0.5 and l was 0.005 μm for individual enzymes and 0.02 μm for 20-member enzyme domains. Note that this movement, unlike the Brownian motion described above, is not dependent on the timestep length Δt (which was always 0.5 ms in our simulations). If a different timestep were to be employed, *k* would have to be adjusted accordingly.

For each timestep, movements are applied in the following order:

1. Brownian motion as in equations 4 and 5
2. Optionally: Tethering between enzymes as in equations 6 – 9
3. Repelling overlapping enzymes

B. Assumptions

The model presented here is intended to be simple, yet capture the essential elements of a diffusion-coupled ETC. Therefore, we made several key assumptions, which are explained below.

1. A simplified bacterial ETC

We model an ETC with only two enzyme types, a dehydrogenase (e.g. succinate dehydrogenase or NADH dehydrogenase) and a terminal oxidase (e.g. cytochrome oxidase). The pair of enzymes is defined by the substrate in which an experiment is carried out. In cases where *E. coli* features redundant enzymes for a function, they are simplified as one type. For example, *E. coli* contains two aerobic oxidases and two NADH dehydrogenase in approximately equal abundances; in each case, the model assumes a single enzyme type whose abundance is the sum, and k_{cat} is the mean, of the two. Individual enzymes exist as single complexes; geometrically these are modeled as circle with a radius of 4 nm and a center which represents its coordinates on the cell surface. To model homotypic enzyme domains (containing 10-50 complexes (*21*)), the radius of these circles is scaled to maintain a constant enzyme area, i.e. radius scaled with the square root of domain size (radius for a 20 enzyme domains is 17.9 nm).

Enzymes are modeled as donating or extracting 2 electrons from a ubiquinone/ubiquinol during each reaction; other electron transfers - oxidation of an electron donor such as NADH, transfer of electrons across enzymes, and reduction of oxygen – are not considered, so are assumed to be much faster than the quinone reactions. The quinone pool is of a single type which can exist in two states (oxidized and reduced), with each particle being defined by the redox state and their coordinates on the cell membrane. The cell surface itself is modeled as a wrapping square plane of 2.5 μm × 2.5 μm with the approximate surface area of an *E. coli* cell (~7.5 μm^2). Auto-oxidation of ubiquinol is assumed to be negligible. For final analysis, the oxidation of two ubiquinols results in the reduction of a single molecule of oxygen.

2. Independent random walks of all ETC components

Each component in the model (enzyme complexes or domains thereof, quinones) undergoes a random walk in the plane. The membrane is therefore assumed to be an ideal, isotropic solvent, with no caging or other localized diffusive effects. The movements of component are independent, so there is an assumption of negligible viscous drag, in which the thermal motion of large complexes in a membrane is expected to carry neighboring lipids with it. Such an effect has been proposed and analyzed in the context of hydrodynamic models (*56*), but has not been tested experimentally. Viscous drag would be expected to increase the effect of diffusion and inhibit overall rates by decreasing substrate mixing.

In the model, random walks are carried out by a Weiner process in which each simulation step results in the movement in both x and y positions of a value randomly chosen through a Gaussian probability distribution whose mean is 0 (i.e. displacement occurs equally in both directions) and whose variance is equivalent to the product of the time step length multiplied by $2D_t$. When the position of any object exceeds the coordinates of the membrane plane, they displace to the opposing edge (wrapping).

Quinone diffusion coefficients are taken from FRAP experiments of NBD-UQ (Fig. 4B in the main text). These measurements depend on a model for relating fluorescence recovery rates to molecular diffusivity, and therefore make assumptions about the geometry of the GEVs (spherical) and a single-exponential fitting of the recovery curve, which is limited by experimental noise and, significantly, by bleaching of the fluorophore at later time points, creating noisy signal where the curves plateau. Additionally, the fluorescent ubiquinone analogue is an imperfect mimic of native *E. coli* Q8, featuring a NBD group and a slightly longer isoprenyl chain (Q10). However, the range of our measured values (~ 0.5 μm^2/s for native lipid

composition) is consistent with reported literature values for similar analogues: Short chain ubiquinones (NBD-Q2), which can be incorporated into live *E. coli* cells, feature diffusion coefficients ~2-3 fold faster (*21*) than our values for NBD-Q10. The ratio between the diffusion of unlabeled long chain (Q8 or Q10) and short chain (Q2) quinones is also factor of two in a system where such measurements have been possible using electrochemical measurements (*57*), so this discrepancy is as expected. Electrochemical measurements (*57*) also did not find significant differences between the diffusion of Q8, native to *E. coli*, and Q10, which was used in our diffusivity measurements, so this is a reasonable analogue.

Enzyme diffusion is extrapolated from diffusivity from ubiquinone diffusivities using the Saffman-Delbrück relationship (*10*), in which diffusion has a weak, logarithmic dependence on object radius. For this calculation, quinones are modeled as circles with a radius of 2.5 nm (*57*) . Enzyme diffusivity (D_{enzyme}) is therefore approximated as a function of measured ubiquinone diffusivity (D_{quinone}), the enzyme/domain radius (r_{enzyme}), and the ubiquinone radius (r_{quinone}, 2.5 nm):

$$D_{enzyme} = \frac{D_{quinone}}{1+ln\left(\frac{r_{enzyme}}{r_{quinone}}\right)} \quad (10)$$

For protein domains, this derivation estimated diffusion coefficients of 0.03-0.1 $\mu m^2/s$, values in line with measurements of ETC complexes (*22*, *58*) and other *E. coli* membrane protein domains (*59*).

The Saffman-Delbrück model has been shown to predict diffusion coefficients of model transmembrane proteins (*60*) and describe the size-diffusion scaling relationship for membrane domains (*61*). However, other measurements of transmembrane protein diffusion have challenged this model, instead proposing a stronger, inverse relationship between protein diameter and diffusion (*62*). It is therefore important to note that enzyme diffusion, within a reasonable range, has only a minor effect on total oxidation rates in our model (Fig. S8C) and we see little difference when switching using these two models. In general, oxidation rates are independent of enzyme diffusion rates unless they are faster than quinone diffusion.

3. ETC complexes act with first-order kinetics

For an enzyme reaction to be diffusion coupled, substrate availability must be limiting relative to activity, i.e. enzymes do not become saturated. Under these conditions, enzyme activity is dependent on substrate concentration and the enzyme's turnover number, k_{cat}. *E. coli* mutants producing low amounts of ubiquinone show a concomitant reduction in respiration rates (*63*), indicating that this is a reasonable assumption despite the high ubiquinone concentration in the inner membrane. Therefore, we can model reactions as stochastic events occurring when a quinone/quinol diffuses within an enzyme's radius with a probability of:

$$P_{rxn} = k_{cat} * \Delta t \quad (11)$$

Under these conditions, respiration rates scale linearly with substrate ubiquinone content (substrate concentration). This feature allows us to scale respiration rates in simulations with a manageable number of electron carriers (generally 10,000 or 50,000) to those of whole cells, which contain ~10-fold more ubiquinones, saving computational bandwidth.

C. Inputs

ETC protein abundances:

Per cell abundances were measured in exponential phase under experimental conditions using quantitative proteomics (Methods and Supplementary Text). Abundances are given as derived number of copies/cell, ± SD.

Succinate respiration (succinate minimal media):

ETC enzyme	Polypeptide	Abundance (copies/cell)
Cytochrome oxidase *bo*	CyoB	311 ± 66
Cytochrome oxidase *bd*-I	CydA	625 ± 93
Succinate dehydrogenase	SdhA	2534 ± 183

NADH respiration (pyruvate minimal media):

ETC enzyme	Polypeptide	Abundance (copies/cell)
Cytochrome oxidase *bo*	CyoB	420 ± 67
Cytochrome oxidase *bd*-I	CydA	686 ± 35
Type I NADH dehydrogenase	NuoF	527 ± 104
Type II NADH dehydrogenase	Ndh	603 ± 83

Enzyme turnover:

Measured k_{cat} values of purified ETC enzymes were taken from the literature. To correct for varying measurement temperature, a temperature correction value was measured in wild-type membrane vesicles using assays for uncoupled enzyme activity using soluble electron donors (TMPD) and acceptors (INT, DCIP) as described in the Methods. These corrections corresponded to Q_{10} temperature coefficients of 1.8 to 3.

Enzyme	Activity (k_{cat}, s^{-1})	Conditions	Source	Measured correction	Activity, 37 °C (s^{-1})
Cytochrome oxidase *bd*-I (Cyd)	642	25 °C, pH 7.0	Kita et. al., 1984 (*64*)	2.7	1747
Cytochrome oxidase *bo* (Cyo)	537	25 °C, pH 7.0	Kita et. al., 1984 (*48*)	2.7	1461
Type I NADH dh (Nuo)	361	23 °C, pH 6.0	Braun et. al., 1998 (*65*)	3.1	1102

Type II NADH dh (Ndh)	1134	30 °C, pH 7.5	Björklöf et. al., 2000 (*66*)	2.0	2267
Succinate dehydrogenase (Sdh)	110	30 °C, pH 8.0	Maklashina et. al., 2006 (*67*)	2.7	300

The corrected k_{cat} values at 37ºC for a given enzyme pair (e.g Sdh and Cyd/Cyo for succinate respiration, Nuo/Nadh and Cyd/Cyo for NADH respiration) are used to determine reaction probability in the simulations, as described above in Eq. 11.

Other physiological parameters:

In order to convert raw simulated respiration rates, e.g. number of quinones out of 50,000 oxidized per simulated time, into comparable cellular respiration rates, e.g. mmol O_2 per hour per gram, dry weight, additional measured and assumed physiological parameters were used: One oxygen molecule becomes reduced for every two ubiquinols oxidized, as is the case for both aerobic terminal oxidases in *E. coli*. The dry weight of a single cell was measured at 0.2 pg for strain BW277832T in succinate minimal media, using a cell counter. The total quinone abundance was measured by HPLC as 2 μmol/g, dw, using hexane extractions from strain BW277832T grown in succinate minimal medium, as previously described (*68*). This abundance corresponds to 600,000 quinones in a cell, or 2-3% of all membrane lipids.

D. Description of Supplementary Movies

Included with this study are a set of movie files visualizing the simulations carried out with the model. In each case, time-dependent output of the model is outputted using Matplotlib as a single image per timestep, which are then compiled into the video. Each frame shows the position of individual particles (ubiquinones, ubiquinols, DHs, TOs) in the whole cell field as well as bulk statistics describing the number of oxidation events (ubiquinols oxidized), the redox state of the quinone pool, and the redox distribution of the quinone pool surrounding TOs. For each movie, the field is displayed with 10,000 quinones; ubiquinols are shown as red points, and ubiquinones are shown as blue points. DHs and TOs enzyme domains are shown as red and blue filled circles, respectively. Upon the oxidation of a ubiquinol, a yellow halo is shown indicating a counted reaction. For all the simulations, the enzyme density and domain size approximates that for NADH respiration in *E. coli*. Each time step represents 0.5 ms. If played at 25 frames per second, the videos are an 80-fold slowed down representation of the simulation. The uploaded versions of these vides (Supplementary Movie S1, S2) contain the first 1 second of a given simulation. Extended versions, which show the respiratory chains reaching a steady state, are available at: https://drive.google.com/open?id=1gQhNv8svxUAZVzsh1UynICtm9eiK0s4l

Methodology for quantitative targeted proteomic analysis of ETC proteins

The SRM targeted proteomic assays were performed, as described previously (*37*), on an Agilent 6460 QQQ mass spectrometer system coupled with an Agilent 1290 UHPLC system (Agilent Technologies, Santa Clara, CA). A Sigma–Aldrich Ascentis Peptide ES-C18 column (2.1 mm × 50 mm, 2.0 μm particle size, operated at 60°C; Sigma-Aldrich) was used to separate

peptides operated at 0.400 mL/min flow rate. Peptides were ionized by using an Agilent Jet Stream source (Agilent Technologies) operating in positive-ion mode with the following parameter settings: Sheath Gas flow=11 l/min, Sheath Gas Temperature=350C, Nozzle Voltage=1000 V, Nebulizing Pressure=30 psi, Chamber Voltage=4500 V.

The custom-synthesized peptides in Table 2 (Genscript) were reconstituted at 1 nmol/μL in 50% acetonitrile containing 0.1% formic acid as stock, and further diluted into 5 fmol/ μL, 10 fmol/ μL, 25 fmol/ μL, 50 fmol/ μL, 100 fmol/ μL, 500 fmol/ μL, and 1 pmol/ μL with diluent of *S. cerevisiae* cell lysate tryptic digest at 2 μg / μL concentration. Ten (10) μL of diluted synthetic peptides and 20 μg sample peptides were separated via a gradient with initial starting condition of 95% buffer A (0.1% formic acid in LC-MS grade water) and 5% buffer B (0.1% formic acid in LC-MS grade acetonitrile), and was increased to 35% over 5.5 min. Buffer B was then increased to 80% over 0.5 min, and held for 1 min at a flow rate of 0.6 mL/min, followed by a ramp back down to 5% B over 0.7 min where it was held for 1.5 min to re-equilibrate the column to original conditions. Selected-reaction monitoring (SRM/MRM) transitions and retention times of targeted peptides were validated by analysis of the synthetic peptides, and a dynamic/scheduled MRM method was developed to monitor a total of 52 transitions with a target cycle time of 0.5 s to yield fewer than 30 concurrent transitions. The generated MS raw data were processed by using Skyline software version 3.70 (MacCoss Lab Software). The titrated measurements of synthetic peptides were fitted by linear regression ($R^2 > 0.99$) to generate standard curve of quantitated peptides. The quantity of these peptides in the samples were calculated based on each standard curve and were exported for further analysis. The SRM methods and data are available at Panoramaweb (*69*) via link: https://goo.gl/JJySak

Chemical synthesis of NBD-X-Q10 used in FRAP experiments

Reagents and equipment: 6-(N-(7-Nitrobenz-2-oxa-1,3-diazol-4-yl)amino)hexanoic acid ("NBD-X") was purchased from Anaspec, Inc. All other reagents were purchased from Sigma. The anaerobic chloroform used was stabilized with amylene. Nuclear magnetic resonance spectra were acquired on a Bruker AVB 400 MHz spectrometer at the UC Berkeley College of Chemistry NMR facility, funded in part by NSF grant CHE-0130862. Chemical shifts are reported in ppm relative to residual solvent signal.

Procedure: A bottle of 0.1 M aqueous HCl was sparged with argon at room temperature while setting up the following reaction. To a 10 mL test-tube at 0 °C was added 86.4mg ubiquinone, 3 mL chloroform, 300 μL methanol and a stir bar. The mixture was sparged with argon for 5 minutes. Roughly 1 mg sodium borohydride was added, and the mixture was stirred under argon. Over the course of 10 minutes, the reaction changed color from yellow to clear. The reaction was quenched with 6 mL sparged 0.1 M HCl, and the organic layer was washed with 6 mL more 0.1M HCl. The organic layer was dried over magnesium sulfate, filtered, and evaporated to dryness under a stream of argon in a test tube with a stir bar. Care was taken to perform all these procedures under an argon atmosphere - ubiquinol re-oxidization has occurred if a yellow color appears. The residue was dissolved in 1mL anaerobic chloroform at 0 °C, and 12mg 4-dimethylaminopyridine (DMAP, 1 equivalent), 29.6mg NBD-X (1 equivalent) and 20.8 μL diisopropylcarbodiimide (DIC, 1.5 equivalent) were added in order. The reaction was stirred at 0 °C and allowed to warm up to room temperature over the course of 8 hours. The reaction mixture was concentrated under a stream of argon, loaded onto a 24 g RediSep Rf Gold silica gel column and eluted in 35% ethyl acetate in hexanes. The fractions containing pure product were

concentrated under reduced pressure repeatedly. Product appears as a viscous orange-red oil with a mass of 24.4 mg (21 % yield).

Product description: The major product at Rf(3:1 hexanes:ethyl acetate) = 0.41 represented a 2.6:1 mixture of the following regioisomers, as quantified by NMR:

3-((2E,6E,10E,14E,18E,22E,26E,30E,34E)-3,7,11,15,19,23,27,31,35,39-decamethyltetraconta-2,6,10,14,18,22,26,30,34,38-decaen-1-yl)-4-hydroxy-5,6-dimethoxy-2-methylphenyl 6-((7-nitrobenzo[c][1,2,5]oxadiazol-4-yl)amino)hexanoate

2-((2E,6E,10E,14E,18E,22E,26E,30E,34E)-3,7,11,15,19,23,27,31,35,39-decamethyltetraconta-2,6,10,14,18,22,26,30,34,38-decaen-1-yl)-4-hydroxy-5,6-dimethoxy-3-methylphenyl 6-((7-nitrobenzo[c][1,2,5]oxadiazol-4-yl)amino)hexanoate

A minor product at Rf(3:1 hexanes:ethyl acetate) = 0.22 has been determined to be NBD-X-methanol (methyl 6-((7-nitrobenzo[c][1,2,5]oxadiazol-4-yl)amino)hexanoate). NBD-X-methanol did not partition into lipid vesicles under the conditions employed in the experiments and therefore no further purification was performed.

NMR analysis: ^{1}H NMR (400 MHz, $CDCl_3$ = 7.26): δ 8.49 (d, J = 8.5 Hz, 1H), 6.27 (s, 1H), 6.22 – 6.13 (m, 1H), 5.75 – 5.64 (m, 1H), 5.18 – 5.03 (m, 9H), 3.91 (s, 3H), 3.80 (s, 3H), 3.53 (dt, J = 11.1, 5.6 Hz, 2H), 3.34 & 3.16 (both d, J = 6.6 Hz, 2H together), 2.71 – 2.59 (m, 2H), 2.15 – 1.53 (m, 79H)

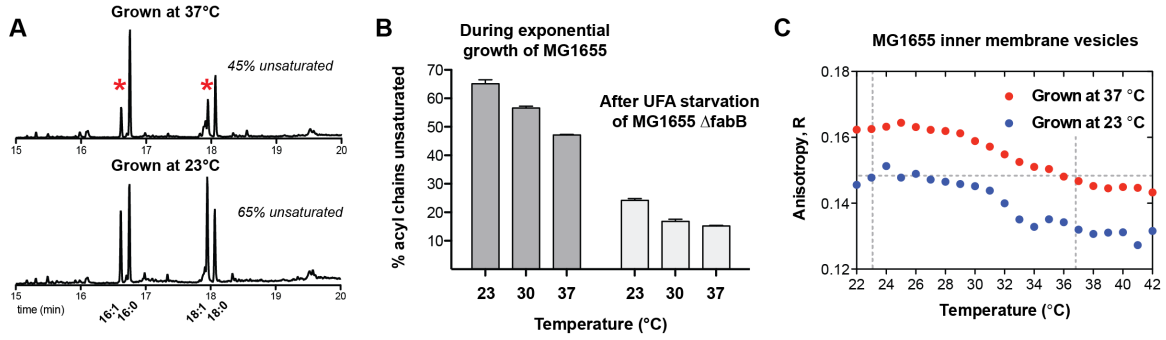

Fig. S1.

Homeoviscous adaptation in *E. coli*. (**A**) Cells grown at differing temperatures (e.g. 37°C vs 23°C) feature varying amounts of unsaturated fatty acids incorporated in membrane phospholipids. Unsaturated species (C16:1 and C18:1) are indicated (red asterisk) in the representative GC-MS chromatograms for cells grown at the given temperature. (**B**) The proportion of acyl chains that are unsaturated decreases with increasing growth temperature. These values are higher than the minimum required unsaturated lipid content needed to maintain growth, as measured using a starving experiment during growth of an unsaturated fatty acid auxotroph. Error bars represent S.E.M. for three independent cultures. (**C**) The relative membrane ordering parameter (R) of the fluidity-probe di-phenyl-hexatriene (DPH), as measured by steady-state fluorescence anisotropy, is maintained at a constant level (dashed line) at both growth temperatures because the changes in lipid unsaturation compensate for the effects of temperature on membrane order.

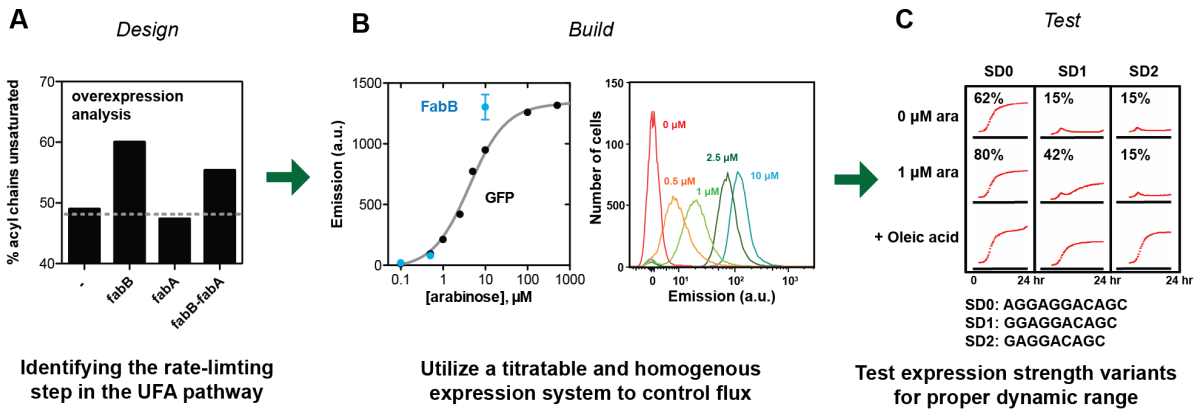

Fig. S2

Using a Design-Build-Test approach to engineer lipid composition in *E. coli*. (**A**) The rate-limiting step in a lipid biosynthetic pathway is identified and targeted. In this case, UFA synthesis in *E. coli* requires two enzymes, FabA and FabB, but only overexpression of *fabB* increases UFA content in a wild-type K12 background. FabB abundance therefore controls saturated vs. unsaturated lipid stoichiometry. (**B**) To systematically manipulate *fabB* expression, a highly titratable promoter (P_{BAD}) is utilized that allows for a ~1000-fold range of expression, as measured using a P_{BAD}-GFP reporter (left). This construct is coupled to a homogenously-inducible strain background (BW277832T), where expression varies consistently on an individual cell basis with inducer concentration, as verified by flow cytometry (right). Rescue of chromosomal *fabB* (Δ*fabB*) by P_{BAD}-*fabB* allows for a wide range of FabB abundance levels (left, blue), as measured by quantitative protein mass spectrometry. Error bars indicate S.D. for biological triplicates. (**C**) A set of P_{BAD}-*fabB* vectors, with varying strength Shine-Delgarno sequences to control translation efficiency, is tested for their ability to manipulate lipid composition above and below the physiological range in a Δ*fabB* background. Shown are growth curves under uninduced (no arabinose), partly induced (1 µM arabinose), and chemically rescued (+ oleic acid, an exogenous UFA) conditions. A SD sequence that is too strong (SD0) features leaky expression in the absence of inducer that prevents titration of fatty acid levels, while one that is too weak (SD2) does not allow for growth except with exogenous UFA. A medium-strength sequence (SD1) allows for titratable UFA content is used for experiments under non-fermentable carbon sources in this study. For growth in glucose media, in which P_{BAD} activity is repressed, the strong (SD0) variant is used.

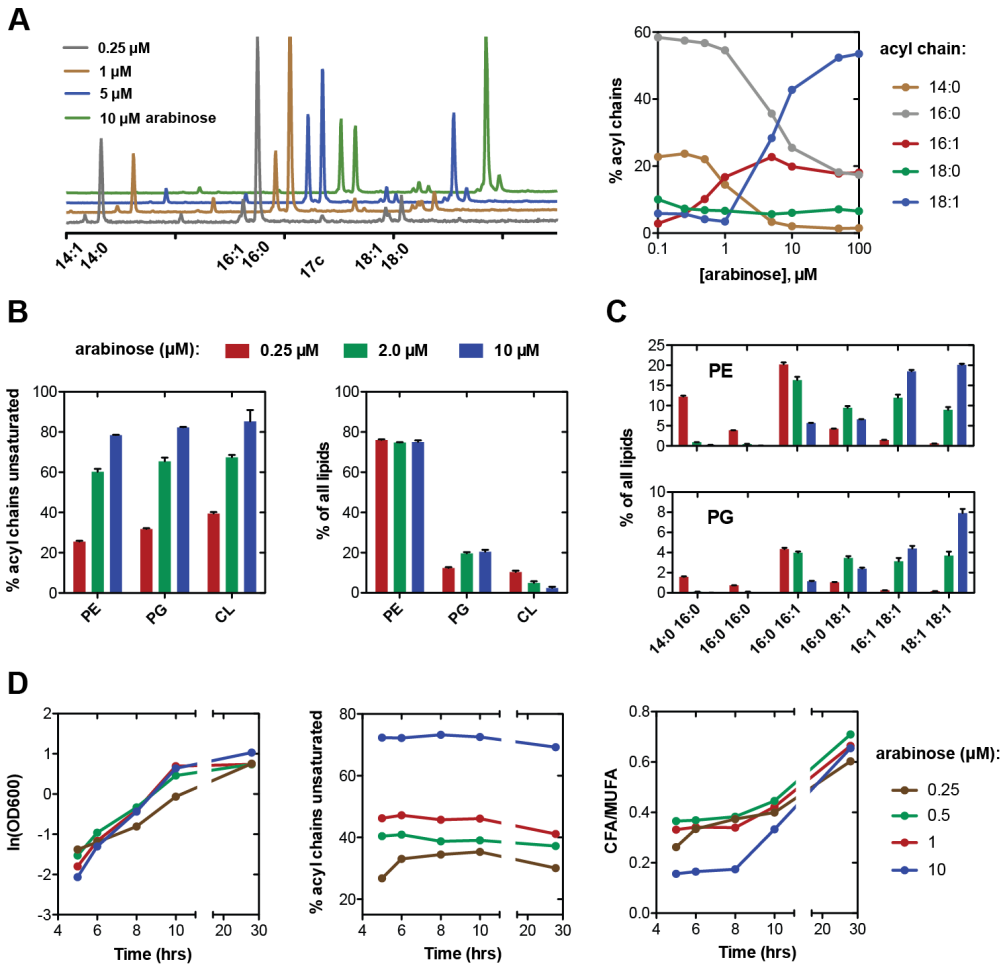

Fig. S3

Lipid analysis of titratable UFA strain. (**A**) Example GC-MS trace of fatty acid methyl esters (FAMEs) generated from titrating *fabB* expression, and therefore UFA synthesis, using the P_{BAD} promoter under various inducer (arabinose) concentrations. This method of analysis is used routinely for experiments in this study. Shown are overlaid chromatograms of the 55 molecular ion, used for quantification, for samples derived from increasing concentration of arabinose. As induction increases, saturated chains (primarily palmitate, C16:0) are substituted with monounsaturated chains (primarily vaccinate, C18:1). Lipids were extracted during exponential phase (OD ~ 0.3) and are representative of the unsaturated lipid profiling routinely used in the study. (**B**) Shotgun MS/MS analysis of intact phospholipid head group and acyl chain composition. Unsaturated lipid titration occurs in the three phospholipid species found in *E. coli*, phosphatidylethanolamine (PE), phosphatidylglycerol (PG), and cardiolipin (CL). PE is the dominant lipid under all conditions (right), while the conversion of PG to CL increases under low UFA levels. Cells were grown under the inducer concentration given in biological triplicate; error bars indicate S.D. (**C**) Analysis for PE and PG sub-species. Increases in arabinose concentration correspond to a substitution of phospholipids with no unsaturated acyl chains (e.g., 16:0, 16:0) or one unsaturated acyl chain (e.g., 16:0 16:1) with ones with two unsaturated acyl chains (e.g. 16:1, 18:1). Cells were grown under the inducer concentration given in biological triplicate; error bars indicate S.E.M. (**D**) Dependence of unsaturated lipid composition on cellular growth stage.

Shown are data for a set of cultures with increasing *fabB* induction (arabinose concentration). As exponential growth progresses (as measured by OD600 readings, left), unsaturated lipid composition stays constant. As cells enter in stationary phase, at 10 hours through 28 hours, cyclopropane fatty acids (CFAs) accumulate and substitute unsaturated fatty acids (right); cells in this state were not used for physiological assays in this study.

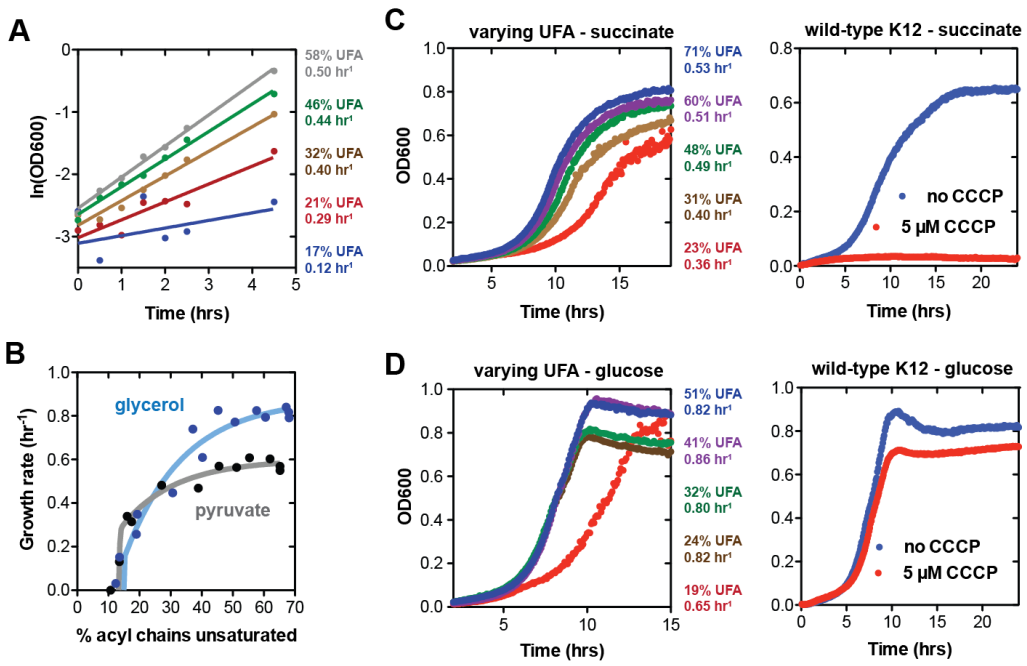

Fig. S4

Features of lipid-dependent physiology in *E. coli.* (**A**) Growth effects of changes to unsaturated lipid content in cells growing in shake-flasks in succinate minimal media. The effect of UFA levels is similar to that in microwell plates otherwise used in this study. (**B**) Cells grown under the non-fermentable carbon sources glycerol and pyruvate exhibit a two-phase dependence of exponential growth rates on unsaturated lipid content, similar to that for succinate (Fig. 2A). (**C**) Aerobic growth on succinate, in which exponential growth rates are modulated by UFA levels (left), is dependent on ATP production from the ETC, so growth is abolished by the addition of the uncoupler CCCP. (**D**) In contrast, microaerobic growth on glucose, in which growth rates above a critical threshold are independent of UFA levels (left), is resistant to PMF uncoupling, since cells generate sufficient ATP for growth from glycolysis.

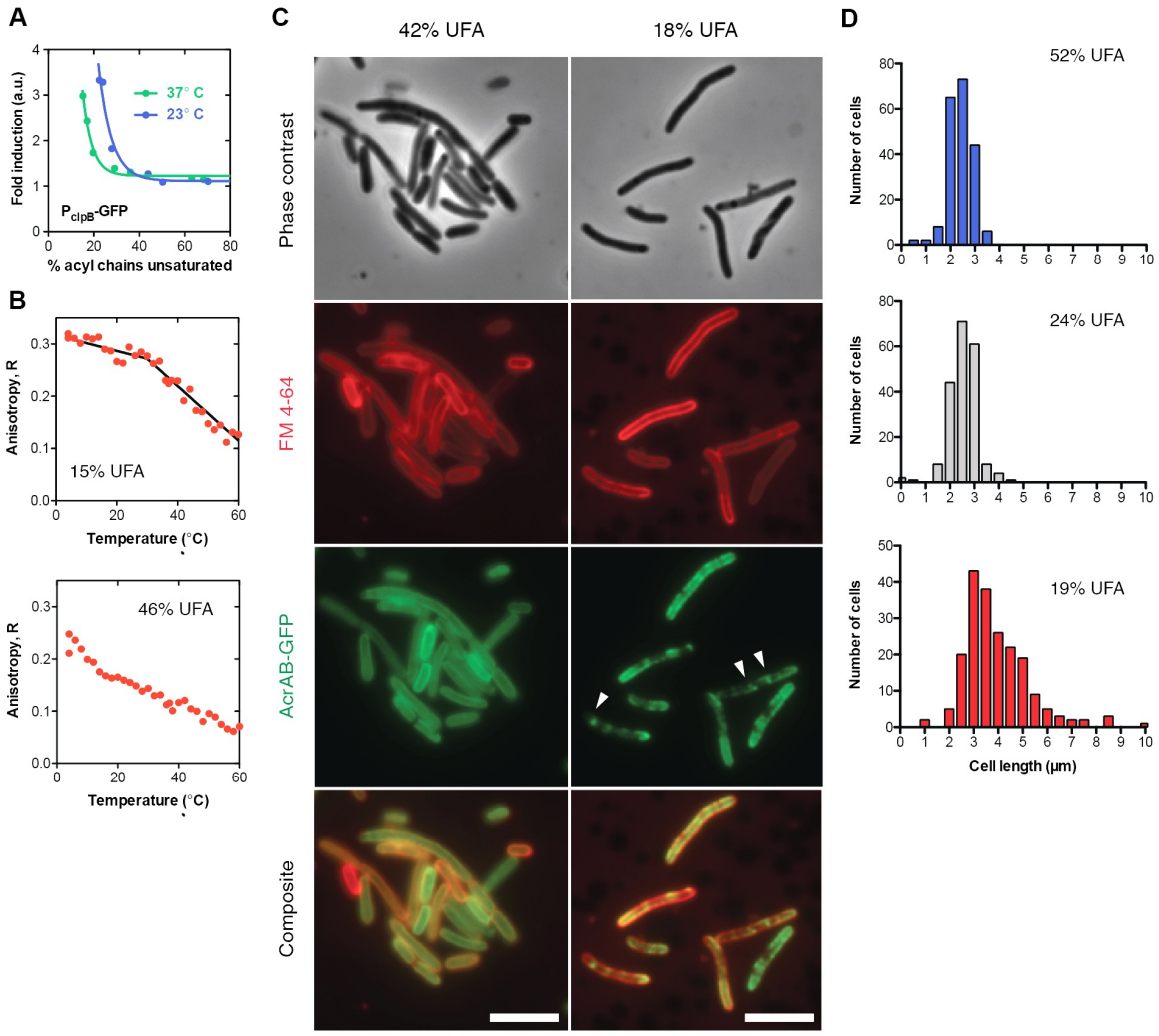

Fig. S5

Low lipid unsaturation triggers envelope stress in *E. coli*. (**A**) HSR induction, as measured by a GFP reporter whose expression is driven by the *clpB* promoter, as a function of lipid unsaturation in cells grown at two different temperatures. HSR induction occurs only as cells approach the minimum lipid unsaturation level at the given growth temperature (~15% at 37º C and ~25% at 23º C, Fig. S1B). Values shown are normalized to those in wild-type K12 cells. (**B**) Membranes extracts from cell in the HSR stress regime show a temperature-dependent phase transitions near the growth temperature (37ºC for 15% UFA), as detected by a plateau in the DPH anisotropy vs. temperature relationship (top). Such phase transitions reflect a change from a disordered to an ordered or gelled membrane state (*70*). In contrast, membranes with high levels of lipid unsaturation (bottom) do not show a phase transition near growth temperatures. (**C**) Fluorescence micrographs of cells at low and intermediate unsaturated lipid contents show defects in membrane protein localization. FM4-64, a lipid dye, is used to stain membranes in the red channel, while a GFP tagged AcrAB, a membrane transporter, is used as a membrane protein reporter in the green channel. Cells with intermediate or high UFA levels show proper co-localization of the membrane protein and lipid dye, while those at low UFA levels (right) show uneven membrane protein localization (patchiness) and cytoplasmic puncta (arrows). Cells are slightly elongated because of

membrane protein overproduction. Scale bars, 5 μm. (**D**) Low UFA levels are associated with elongated cell lengths, indicative of defects in cell division machinery. Histograms show the distribution, taken from phase contrast imaging of 200 unlabeled cells, with high, intermediate, or low unsaturated lipid contents. Significant cell elongation occurs only with low lipid unsaturation, where a HSR is induced.

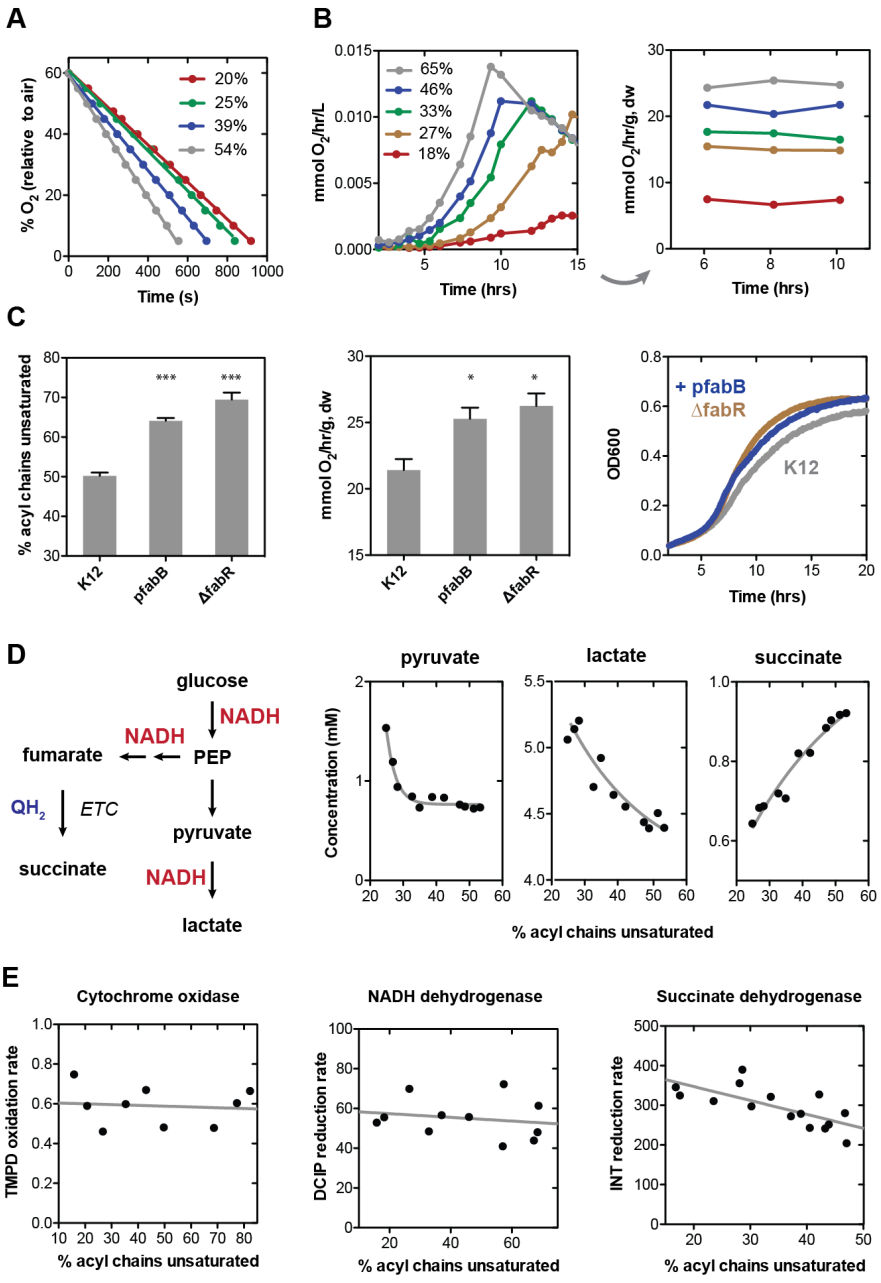

Fig. S6

Features of lipid-dependent respiratory metabolism. (**A**) Clarke electrode measurements of UFA-dependent respiratory activity in succinate minimal media. Increasing lipid unsaturation causes more rapid consumption of the initially aerated media, but oxygen depletion (respiration) rates show a linear decrease ($R^2 > 0.99$) in all conditions until below 5% of atmospheric levels. Oxygen levels within this range therefore do not affect respiratory rates, indicating that oxygen uptake by diffusion is not rate limiting for respiration under aerobic conditions. (**B**) UFA-dependent respiration rates stay constant during exponential growth. Shown are oxygen uptake data from a RAMOS shake flask experiment with cells growing under different *fabB* induction levels, with average UFA-levels shown (left). At three different time points, cells were sampled for lipid composition and optical density, and oxygen uptake was converted to respiratory rates (right). (**C**)

Increased UFA levels (left) in wild-type K12 cells (MG1655), either through plasmid-based *fabB* overexpression (pfabB) or deletion of the negative regulator *fabR* (ΔfabR) also increase uncoupled respiration rates (middle) and exponential growth rates (right) in succinate. Error bars indicate S.E.M., n = 3. Overlaid are results from two-tailed t-tests comparing rates to that of unperturbed cells; *, $p < 0.05$, ***, $p < 0.001$. (**D**) Effects of unsaturated lipid composition on mixed acid fermentation, whose reactions are diagrammed (left). Low UFA levels increase the accumulation of pyruvate, indicating an inhibition of post-glycolytic oxidation, and its NADH-consuming fermentation product, lactate. In contrast, succinate accumulation, which requires the activity of the ETC enzyme fumarate reductase (FR) and ubiquinol as an electron donor, is inhibited by low UFA levels. Although growth is not affected by changes in UFA levels in this regime (Fig. 2A, bottom), the accumulation of lactate indicates an accumulation of NADH, while succinate depletion is consistent with reduction in FR activity. Other explanations for succinate depletion – such as to maintain the NAD^+/NADH ratio – are also possible. (**E**) The activities of ETC enzymes are unaffected by UFA levels when utilizing soluble donor or acceptors, indicating that enzyme activities per se are not responsible for the effect of lipid composition on respiration. Cytochrome oxidase activity was measured by TMPD oxidation and is expressed as the increase in absorbance at 611 nm for 5 mM TMPD incubated with 0.2 mM ascorbate and membrane vesicles (5 μg of protein). NADH dehydrogenase activity was measured by DCIP reduction and is expressed as decrease in absorbance at 600 nm per hour for 50 μM DCIP incubated with 125 μM NADH and membrane vesicles (1 μg of protein). Succinate dehydrogenase activity was measured by INT reduction and is expressed as increase in absorbance at 500 nm per minute for 2 mM INT incubated with 20 mM sodium succinate and washed cells (50 μg dry weight).

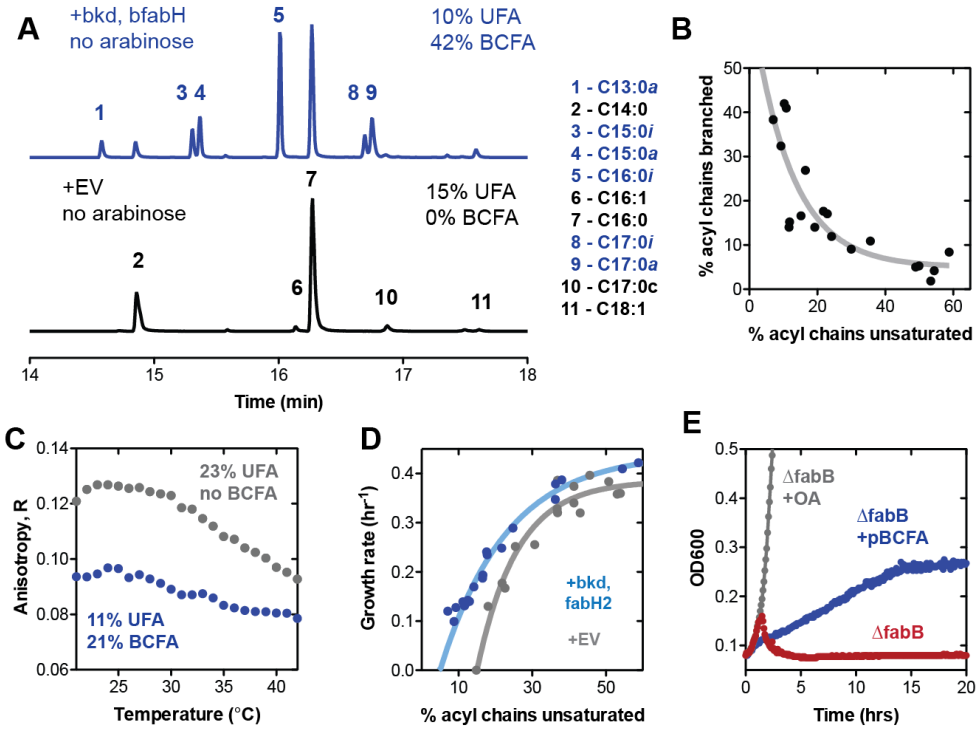

Fig. S7

Physiological effects of heterologous incorporation of BCFAs into *E. coli* membranes. (**A**) GC-MS chromatograms (74 molecular ion) that show branched chain lipid synthesis in *E. coli*. A plasmid for BCFA production was constructed using six genes (*fabH2* and the five-gene *bkd* operon) from *B. subtilis*, which uses branched chain phospholipids to maintain membrane fluidity. An UFA-titratable strain was grown with the plasmid in amino acid supplemented media in the absence of *fabB* induction (no arabinose), from which esterified fatty acids were analyzed. Peaks highlighted in the top chromatogram are branched fatty acid derivatives not present in the empty vector control (EV). Lipid species were identified by fragmentation patterns and are listed to the right; *i* and *a* indicate *iso* and *anteiso* BCFA species, respectively, while *c* indicatse cyclopropane FAs. (**B**) The dependence of BCFA production on UFA content in *E. coli*. UFA content was modulated by growing cells with various amounts of arabinose. Cells with low levels of UFA were enriched in BCFA. (**C**) DPH anisotropy of membrane vesicles generated from BCFA-enriched cells (blue) show a lower membrane ordering as compared to BCFA-free cells that have higher UFA levels, confirming that BCFA's can orthogonally fluidize *E. coli* membranes. (**D**) The effect of BCFA incorporation on exponential growth rates in succinate rich media. BCFAs increase growth rates compared to the empty vector (EV) control, especially under low UFA levels, consistent with their effect on respiratory rates (Fig. 2D). (**E**) In the complete absence of UFA synthesis, BCFAs prevent saturated lipid-induced cell lysis. Cells with a ΔfabB background cannot synthesize UFAs and are generally maintained on oleic acid (OA) containing media. When these are diluted into OA-free media, as shown, cells grow until their initial UFA pool becomes diluted, upon which lysis occurs, as shown by a drop in OD (red). BCFA synthesis (blue) prevents lysis and allows cells to continue growing until UFA content reaches ~6%. This much lower limit, compared to 15% in the absence of BCFAs, likely corresponds to fluidity-independent role for UFAs in cell growth.

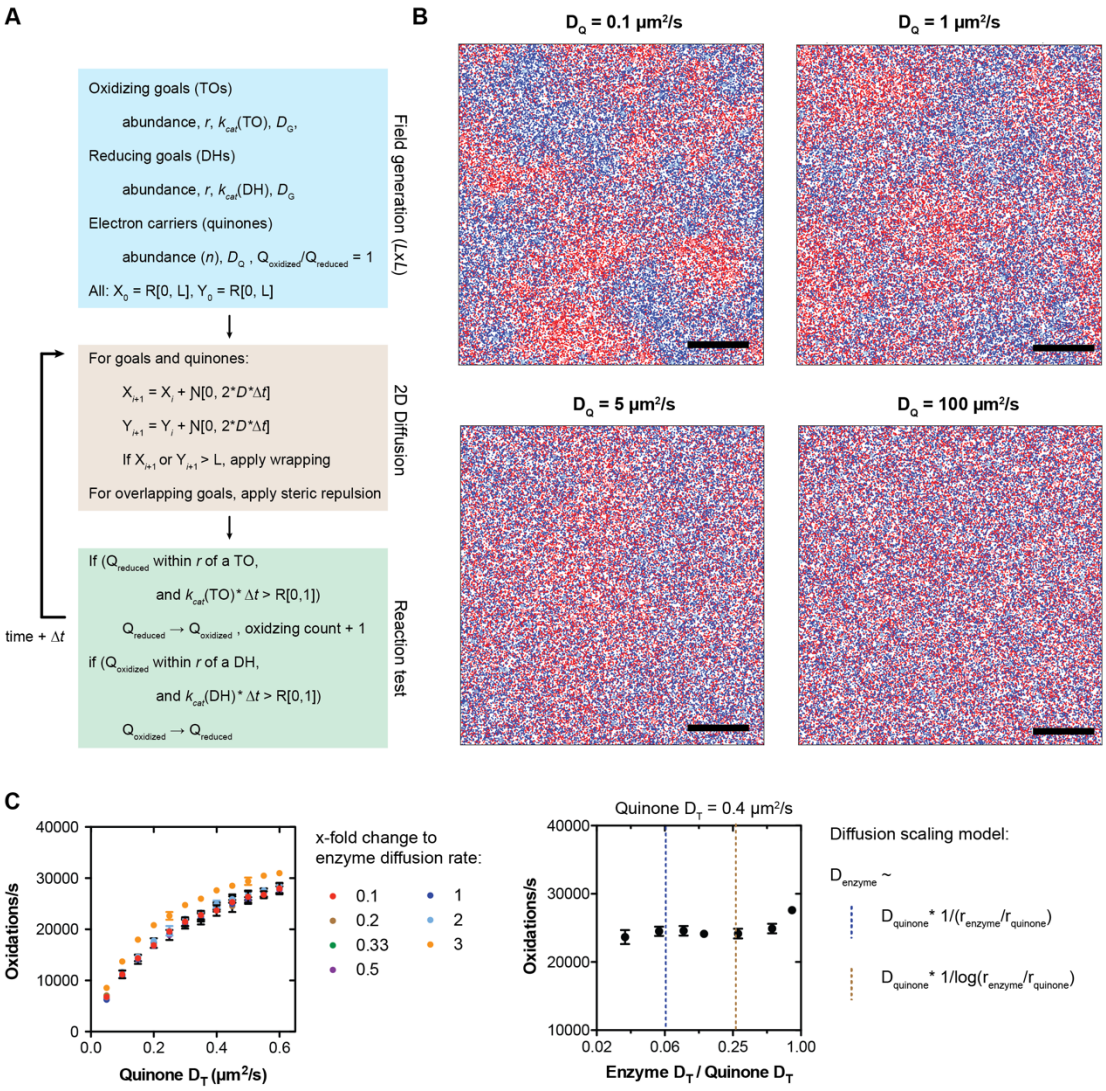

Fig. S8

Simulated effects of diffusion on a collision-coupled ETC. (**A**) Overview of the reaction model employed in this study. In summary, a random field of ubiquinones, ubiquinols, DH enzymes, and TO enzymes are generated based on experimentally measured abundances. These particles undergo Brownian motion, which is simulated as a Wiener process where diffusivity determines the step size during a random walk. At each time-step, any ubiquinones co-localizing within the radius of a DH and any ubiquinols co-localizing within the radius of a TO, can interconvert, with the probability of reaction based on the k_{cat} of the specific DH or TO. When a ubiquinol undergoes oxidation, ½ of an oxygen molecule is consumed. (**B**) The effect of ubiquinone diffusivity on the mixing of the quinone pool. Shown are whole-cell fields of 50,000 quinones, with oxidized species in blue and reduced species in red. When diffusion is slow (e.g. 0.1 $\mu m^2/s$, corresponding to low UFA levels), these species cluster in patches that correspond to statistical locations of DH and TO enzyme domains because of poor mixing. As diffusion increases, these anisotropies diminish, indicating that the system is becoming less diffusion limited. At very high diffusivities (100 $\mu m^2/s$), which are not physiological, the system is well-mixed and diffusion does not affect rates. Scale bar, 500 nm. (**C**) In contrast to ubiquinone, enzyme diffusion rates have little effect on

respiration rates. (Left) Oxidation rates for a typical set of simulations as a function of ubiquinone diffusivity with different corrections to the enzyme diffusion correlation as described in the Supplemental Text. A value of one corresponds to the Saffman-Delbrück relationship, while lower or higher values indicate that enzymes are slowed down or sped up, respectively. (Right) Data for a single ubiqunione diffusivity, corresponding to the value for wild-type cells. As enzyme diffusivity changes, the oxidation rate is constant as long as enzymes diffuse slower than the electron carriers. Dashed lines indicate the diffusivity ratio for the weak Saffman-Delbrück relationship (brown) for extrapolating enzyme diffusion and a stronger inverse relationship (blue), as described in the Supplemental Text.

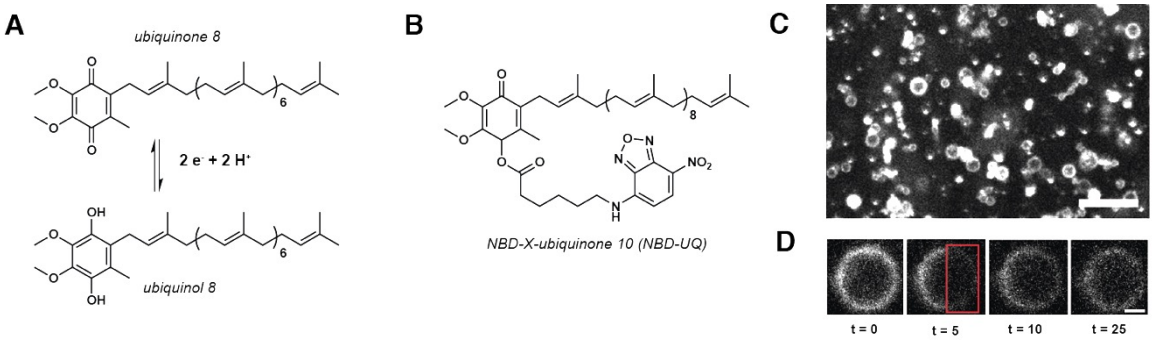

Fig. S9

A fluorescent probe to measure ubiquinone diffusion. (**A**) The structure of the primary aerobic electron carrier in *E. coli*, ubiquinone 8, is shown alongside its reduced form, ubiquinol 8. (**B**) The structure of a fluorescently labeled ubiquinone, NBD-X-ubiquinone 10 or NBD-UQ, that was synthesized to measure the UFA-dependence of ubiquinone diffusivity for this study. (**C**) Labeling of *E. coli* GEVs with NBD-UQ. Scale bar represents, 10 µm. (**D**) Example of a FRAP experiments measuring NBD-UQ diffusion in GEVs. The highlighted box was bleached before the t = 5 (seconds) images. Scale bar, 2 µm.

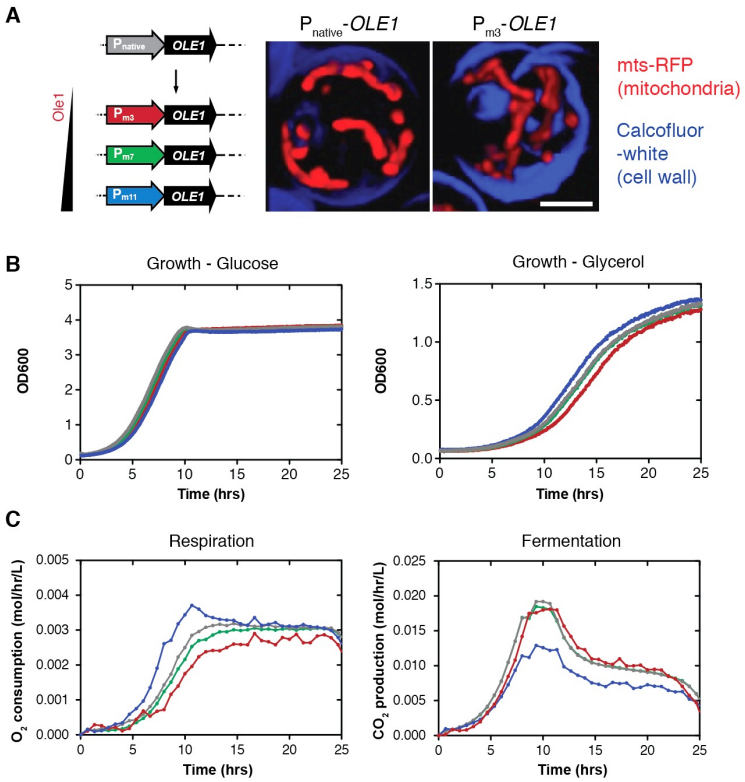

Fig. S10

Lipid unsaturation mediates respiratory metabolism in budding yeast. (**A**) Substitution of the *OLE1* promoter with a set of *TEF1* promoter mutants allows for modulation of lipid unsaturation in budding yeast. In this range of promoter strengths, cells maintain their mitochondrial morphology. Images show reconstructions from confocal z-stacks of cells harboring a mitochondrial-targeted RFP (mts-RFP, red). Mitochondria of the weakest OLE1 promoter mutant (P_{m3}) show tubular mitochondria characteristic of wild-type (P_{native}) cells. Calcofluor-white staining of the cell wall and bud scars (blue) is used to delineate the cellular boundary for clarity. Scale bar, 2 µM. (**B**) All strains grew to same final OD and feature similar growth rates in fermentable media with glucose as the carbon source (left). Higher unsaturated lipid content, however, led to faster growth in non-fermentable media with glycerol as the carbon source (right). Growth curves are color coded according to the promoters in panel A. (**C**) Oxygen consumption (left), measured with a RAMOS system, increases with increasing lipid unsaturation, demonstrating faster respiration rates. The corresponding carbon dioxide production rates for the same experiment show that fermentation activity is unaffected or is decreased by increasing lipid unsaturation. Cells were grown in shake flasks in minimal media with glucose. Respiration and fermentation traces are color coded according to the promoters in panel A.

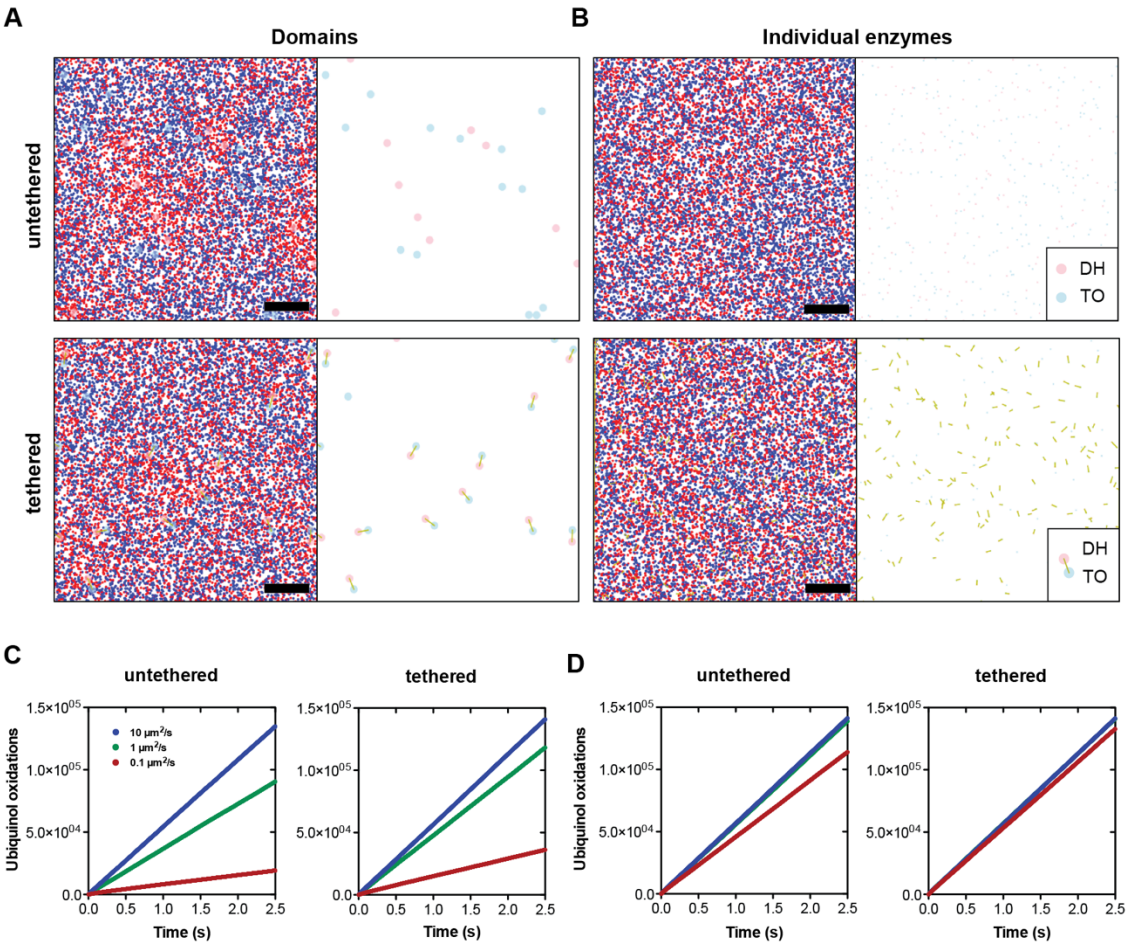

Fig. S11

Simulated effects of topological organization on a diffusion-coupled ETC. (**A**) and (**B**) Anisotropies in the ubiquinone (blue) and ubiquinol (red) distributions during *E. coli* respiratory simulations. Shown are example particle fields in ETC simulations side by side with the corresponding field without the quinones, in order to highlight enzyme localization. The sample enzyme pair (*E. coli* Nuo/Ndh DH and Cyo/Cyd TO) are modeled as either as homotypic domains of 20 enzymes (**A**), approximating the *E. coli* ETC, and as individual enzymes (**B**). In addition, potential interactions between DH and TOs are modeled using a spring tethering function (bottom), which in the case of individual enzymes mimics the organization observed for some mitochondrial ETC enzymes. Scale bars are 200 nm and inserts for the individual enzymes show a 5x magnification. (**C**) and (**D**) The anisotropies in the quinone distribution corresponds to changes in the rate of ubiquinol oxidations, i.e. ETC flux. Shown are time courses of whole cell simulations for three different quinone diffusivities; 0.1, 1.0, and 10 $\mu m^2/s$ with domain organization (**C**) or individual enzymes (**D**). Actual ubiquinone diffusivities fall within the two lower values, while the higher value mimics a well-mixed system. As compared to individual enzymes, homotypic domains increase quinone anisotropy and reduce reaction rates because of increases in the average distance between a DH and TO, given the same total number of enzymes. In contrast, enzyme tethering reduces this distance through direct affinity, thus decreasing the anisotropy of the quinone pool and increasing respiration rates.

Table S1.

List and description of bacterial strains used in this study.

Name	Genotype	Source	Notes
MG1655	F- lambda- *ilvG*- *rfb*-50 *rph*-1	CGSC	Wild-type K12 strain
BW27783 2T	rrnB3, ΔlacZ4787, hsdR514, Δ(araBAD)567, Δ(rhaBAD)568 ΔaraFGH, Φ(ΔaraEp PCP8 ±araE), ΔendA, lacY A177C	Mark A. Kay et. al. 2010	Bacterial strain for homogenous expression from PBAD
fabB	BW27783 2T, fabB::CAT	This study	Bacterial UFA auxotroph, is maintained with oleic acid supplementation
UFA1	BW27783 2T, fabB::CAT, pBAD30-SD1-fabB	This study	Bacterial strain for titratable UFA content in non-fermentable media
UFA2	BW27783 2T, fabB::CAT, pBAD30-SD0-fabB	This study	Bacterial strain for titratable UFA content in glucose media
MG1655 HSR	MG1655, pBbBk-PclpB-GFP	This study	K12 background with a HSR reporter plasmid
UFA1 HSR	UFA1, pBbBk-PclpB-GFP	This study	*E. coli* strain for analyzing induction of HSR
UFA1 AcrAB	UFA1, pBbB5k-AcrAB-GFP	This study	*E. coli* strain for analyzing lmembrane protein localization
UFA1 BCFA	UFA1, pBbB5k-AcrAB-GFP	This study	*E. coli* strain for heterologous synthesis of BCFAs
CYO2	UFA1, pBbA1a-SD2-cyoABCD	This study	*E. coli* strain for modulation of cytochrome *bo* oxidase

Table S2.

List and description of yeast strains used in this study.

Name	Genotype	Source	Notes
W303-1A	*MAT*a *leu2-3,112 trp1-1 can1-100 ura3-1 ade2-1 his3-11,15*	ATCC	S288C background strain
m3-OLE1	W303a, *ole1*::pTEF1m3-*OLE1*	This study	Weak constitutive promoter driving *OLE1* expression
m7-OLE1	W303a, *ole1*::pTEF1m7-*OLE1*	This study	Medium-strength constitutive promoter driving *OLE1* expression
m11-OLE1	W303a, *ole1*::pTEF1m11-*OLE1*	This study	Strong constitutive promoter driving *OLE1* expression

Table S3.

List of synthetic peptides used in this study.

ETC enzyme	Target	Peptide sequence
Cytochrome oxidase *bo*	CyoB	APGMTMFK
Cytochrome oxidase *bd*-I	CydA	SVDTPVIGLK
Succinate dehydrogenase	SdhA	VTGQALTVNEK
Complex I NADH dehydrogenase	NuoF	GGAGFSTGLK
Type II NADH dehydrogenase	Ndh	DIGGLETNR

Movie S1

Simulation of NADH-linked respiration with slow ubiquinone diffusion (0.1 $\mu m^2/s$). These conditions represent the lower range of acyl chain unsaturation (~20%) sampled in this study. Solid points represent interconverting ubiquinone (blue) and ubiquinol (red) species. Larger, translucent filled circles represent terminal oxidases (blue) and dehydrogenases (red). Yellow filled circles are used to highlight when an oxidation of a ubiquinol occurs. Respiration in this case is strongly diffusion limited, as shown by the patchy ubiquinone/ubiquinol distributions in the field and the statistical depletion of ubiquinol near TOs (shown in the bottom left). When played at 25 frames per second, the movie represents an 80-fold slowed down representation of the simulation.
A longer version of the movie is available at:
https://drive.google.com/open?id=1gQhNv8svxUAZVzsh1UynICtm9eiK0s4l

Movie S2

Simulation of NADH-linked respiration with slow ubiquinone diffusion (0.1 $\mu m^2/s$) and enzyme tethering. In this case, individual DH and TO domains become tethered as the simulation progresses, using an attraction function described in the SI. Tethering is highlighted with yellow line between the center of the DH and TO. Tethering allows for a more homogenous ubiquinone/ubiquinol distribution in the field, shown the distribution of ubiquinol as a function of distance from TOs (shown in the bottom left), even with slow ubiquinone diffusion. When played at 25 frames per second, the movie represents an 80-fold slowed down representation of the simulation.
A longer version of the movie is available at:
https://drive.google.com/open?id=1gQhNv8svxUAZVzsh1UynICtm9eiK0s4l